STATIC AND DYNAMIC AEROELASTIC ANALYSIS OF A VERY LIGHT AIRCRAFT

A THESIS SUBMITTED TO
THE GRADUATE SCHOOL OF NATURAL AND APPLIED SCIENCES
OF
MIDDLE EAST TECHNICAL UNIVERSITY

BY

HALİME GÜL DEMİRER

IN PARTIAL FULFILLMENT OF THE REQUIREMENTS
FOR
THE DEGREE OF MASTER OF SCIENCE
IN
AEROSPACE ENGINEERING

SEPTEMBER 2021

Approval of the thesis:

STATIC AND DYNAMIC AEROELASTIC ANALYSIS OF A VERY LIGHT AIRCRAFT

submitted by **HALİME GÜL DEMİRER** in partial fulfillment of the requirements for the degree of **Master of Science in Aerospace Engineering Department, Middle East Technical University** by,

Prof. Dr. Halil Kalıpçılar
Dean, Graduate School of **Natural and Applied Sciences**

Prof. Dr. İsmail Hakkı Tuncer
Head of Department, **Aerospace Engineering**

Prof. Dr. Altan Kayran
Supervisor, **Aerospace Engineering, METU**

Examining Committee Members:

Prof. Dr. Demirkan Çöker
Aerospace Engineering, METU

Prof. Dr. Altan Kayran
Aerospace Engineering, METU

Prof. Dr. Ozan Tekinalp
Aerospace Engineering, METU

Prof. Dr. Dilek Funda Kurtuluş
Aerospace Engineering, METU

Assist. Prof. Dr. Turaç Farsadi
Mechanical Engineering, ATU

Date:10.09.2021

I hereby declare that all information in this document has been obtained and presented in accordance with academic rules and ethical conduct. I also declare that, as required by these rules and conduct, I have fully cited and referenced all material and results that are not original to this work.

Name, Surname: HALİME GÜL DEMİRER

Signature :

ABSTRACT

STATIC AND DYNAMIC AEROELASTIC ANALYSIS OF A VERY LIGHT AIRCRAFT

DEMİRER, HALİME GÜL
M.S., Department of Aerospace Engineering
Supervisor: Prof. Dr. Altan Kayran

September 2021, 90 pages

Aircraft design processes need to ensure that the aircraft is aeroelastically stable within its operational envelope. This thesis presents an overview of the static aeroelastic, flutter and gust response analysis of a very light aircraft. MSC.FlightLoads and MSC.Nastran are used for aeroelastic modeling and analysis. The methods to be used in the aeroelastic analysis of the VLA are tested on the AGARD 445.6 wing, and the results are in good agreement with the literature. Aeroelastic model corrections such as improvement of the aerodynamic solution, examining different aerodynamic modeling and aero-structure coupling approaches are implemented. Aerodynamic calculations are based on the Doublet-Lattice Method (DLM), which is the aerodynamic theory employed by Nastran for subsonic flows. The aerodynamic solution is improved by including the camber and the angle of incidence of the wing through the addition of an initial downwash. DLM-based loads are compared with loads obtained from computational fluid dynamics (CFD) analysis. The effects of DLM correction on the static aeroelasticity outputs are discussed. It is revealed by dynamic aeroelastic stability analysis that there is no flutter issue within the flight envelope. Matched point flutter solutions for various aileron stiffness are presented. Finally, the vertical acceleration response of the vehicle and internal structural response to the 1-cosine gust are analyzed. It is shown that the gust encountered at the cruise speed condition results in a higher vertical acceleration response than the limit maneuver load factors. Furthermore, tuned gust response analysis is conducted by tuning the gust velocity for different gust gradient lengths. Slightly higher responses than those found for the single gust gradient length required by CS-VLA [1] are captured at a shorter gradient length. Dynamic response analysis reveals that the response of the aircraft dies out in a short time and the model shows a dynamically stable behavior.

Keywords: aeroelasticity, very light aircraft, finite element analysis

ÖZ

ÇOK HAFİF BİR UÇAĞIN STATİK VE DİNAMİK AEROELASTİK ANALİZLERİ

DEMİRER, HALİME GÜL
Yüksek Lisans, Havacılık ve Uzay Mühendisliği Bölümü
Tez Yöneticisi: Prof. Dr. Altan Kayran

Eylül 2021 , 90 sayfa

Uçak tasarım süreçlerinde, uçağın operasyonel kapsamı içinde aeroelastik olarak stabil olduğunun gösterilmesi gerekir. Bu tez, çok hafif bir uçağın statik aeroelastik, çırpınma ve rüzgar tepkisi analizine genel bir bakış sunar. Aeroelastik modelleme ve analiz için MSC.FlightLoads ve MSC.Nastran kullanılır. İncelenen hava aracının aeroelastik analizinde kullanılacak yöntemler, AGARD 445.6 kanadında test edilmiş olup, literatür ile uyumlu sonuçlar elde edilmiştir. Aerodinamik çözümün iyileştirilmesi, farklı aerodinamik modelleme ve aero-yapı birleştirme yaklaşımlarının incelenmesi gibi aeroelastik model düzeltmeleri uygulanmaktadır. Aerodinamik hesaplamalar, Nastran tarafından ses altı akışlar için kullanılan aerodinamik teori olan Doublet-Lattice Metodu'na (DLM) dayanmaktadır. Aerodinamik çözüm, ilk akıma aşağı doğru sapma ekleme yoluyla, kamber ve kanadın geliş açısı dahil edilerek iyileştirilir. DLM metoduna dayanan yükler, hesaplamalı akışkanlar dinamiği (HAD) analizinden elde edilen yükler ile karşılaştırılmış ve DLM düzeltmesinin statik aeroelastisite çıktıları üzerindeki etkileri tartışılmıştır. Dinamik aeroelastik stabilite analizi ile uçuş zarfı içerisinde herhangi bir çırpınma sorununun olmadığı gösterilmiştir. Farklı kanatçık dönüş sertliği için çırpınma çözümleri sunulmaktadır. Son olarak, uçağın 1-kosinüs profilindeki ani rüzgara karşı dikey ivme tepkisi ve iç yapısal tepkisi analiz edilir. Seyir hızı koşulunda karşılaşılan ani rüzgarın, limit manevra yük faktörlerinden daha yüksek bir dikey hızlanma tepkisi ile sonuçlandığı gösterilmiştir. Ayrıca, farklı sağanak rüzgar gradyan uzunlukları için rüzgar hızının büyüklüğü ayarlanarak dinamik tepki analizleri tekrar edilmiştir. CS-VLA [1] tarafından gerekli görülen tek rüzgar gradyan uzunluğu için bulunanlardan bir miktar daha yüksek tepkiler, daha kısa bir gradyan uzunluğunda tespit edilmiştir. Dinamik tepki analizi, uçağın tepkisinin kısa sürede sönümlendiğini ve modelin dinamik olarak kararlı bir davranış gösterdiğini ortaya koymaktadır.

Anahtar Kelimeler: aeroelastisite, çok hafif hava aracı, sonlu elemanlar analizi

To my family...

ACKNOWLEDGMENTS

First of all, I would like to express my gratitude to my supervisor Prof. Dr. Altan Kayran for his time, guidance and invaluable support throughout this study. It has been my chance having the opportunity of working with him. Beyond this thesis work, I will always take his dedication and motivation a model on myself.

This study examines the model of the METU-VLA project, which is being conducted in cooperation with Turkish Aerospace Industry. I would like to thank TAI for supporting this project. In addition, for their work and collaboration, I owe thanks to project members who prepared the global finite element model and made the CFD analysis.

I wish to thank my dear friend Dilek Güzel for her valuable friendship and support.

I sincerely thank Can Erdoğan, who has always been there for me and supporting me. He was really helpful with his insight and valuable advice.

Finally, I am deeply grateful to my beloved family, my parents Handan Demirer and Ali Demirer, and my sister Zeynep Demirer for their love, support and encouragement.

TABLE OF CONTENTS

CHAPTERS

LIST OF TABLES

TABLES

LIST OF FIGURES

FIGURES

CHAPTER 1

INTRODUCTION

Aeroelasticity studies the interaction between aerodynamic, elastic and inertial forces acting on a structure. It branches into two as static and dynamic aeroelasticity. The static part examines the interaction between deflections of flexible structures and the aerodynamic loads where the forces and motions are assumed to be constant in time. Static aeroelastic deformations govern the loads in steady flight conditions. Static stability and control characteristics and the trim behavior of the aircraft are also affected by static aeroelastic phenomena. The main topics of this branch are load distribution, divergence, control surface effectiveness and control system reversal. Load distribution refers to the influence of elastic deformations of structure on the aerodynamic pressure distribution over the structure. Divergence is a static instability of a lifting surface that occurs when the moments due to aerodynamic forces overcome the restoring moments due to structural stiffness. The most common type is the wing torsional divergence. Control surface effectiveness points out a reduction of the effectiveness of the control surfaces due to structural deformations. In other words, aeroelastic interactions affect the controllability of the air vehicle. Control effectiveness reduces with the increasing speed until a critical point called reversal speed. At reversal speed, no response is received from displacing a control surface. Beyond the reversal speed, airplane responses in the opposite of the intended direction. This is known as control reversal.

In dynamic aeroelasticity, inertial forces are involved as well as aerodynamic and elastic forces. In this case, aerodynamic forces are under dynamic motion. Therefore, unsteady aerodynamic effects need to be considered. The subjects of interest are flutter, buffeting and response to dynamic loadings. Flutter indicates a dynamically unstable condition in which the structure extracts energy from the air stream [2]. Flutter is an unstable self-excited vibration of an elastic structure exposed to the airstream. It is a widely studied phenomenon in aeroelasticity since it generally results in catastrophic structural failure. Below a critical speed, called the flutter speed, an initial disturbance leads to stable oscillations in the system. At the flutter speed, the amplitude of oscillation neither decays nor grows. Above the flutter speed, one of the vibrational modes becomes negatively damped and diverging oscillations occur. Buffeting refers to high frequency vibrations when a component of the vehicle is subjected to the wake of another component or an aircraft flies in the wake of another aircraft [3]. Dynamic response denotes the transient response of the structure to rapidly applied loads. Sources of rapidly applied loads can be gusts, landing forces, rapid maneuvering, dropping of external stores, etc. In the case of dynamic loading, aeroelasticity plays a role both in the overall response of the airplane and in the internal stress in the structure.

Although the term aeroelasticity was used first in the early 1930s by two British engineers Pugsley and Cox, aeroelastic problems have influenced air vehicle design since the beginning of the powered flight. [4] reviews the historical background of aeroelastic problems causing new requirements, design features and a tendency to certain design options in aviation. For instance, in 1903, Professor Langley's monoplane had crashed just 9-day before Wright Brother's first manned, powered flight. The reason behind Langley's failure can be explained by the phenomena known today as wing torsional divergence. The failure of Langley's monoplane versus the success of Wright's biplane had an influence on aircraft designers' preference in favor of biplanes for years. Then, in 1916, the tail flutter of the Handley Page O/400 bomber was the first recorded flutter problem to be modeled and solved [5, 6]. The solution was using torsionally stiff connections between the left and right elevators, and it has been a design feature. In 1918, during the development of the Fokker D-8, which was a high wing cantilevered monoplane, wing failures occurred in high speed dives. The cause of the failure was discovered as wing torsion resulted from an increase in the angle of incidence at the wing tip with increasing load. This case is an unfortunate example of the consequences of load redistribution due to static aeroelastic effects. Moreover, wing-aileron flutter was observed in D-8 and some monoplane racers of the 1920s and 1930s. Statically balancing the ailerons about the hinge-line has been applied as a solution and precaution for this problem.

Historical cases have shown that aeroelastic problems can lead to loss of design effectiveness or even catastrophic failures. Serious researches were conducted to understand the mechanism behind the encountered problems. Aeroelasticity has been a complex, interactive field of research expanding its scope over time, studying new challenges posed by developments in the aerospace industry. Besides, regulations have been introduced to ensure that aircraft are designed to be aeroelastically stable and aircraft loads are properly accounted for the deflection of the structure. Today, considering aeroelastic effects in aircraft design processes and making analyzes to understand the aeroelastic characteristics of the design has become a standard and essential procedure.

As in all aircraft to be certified, aeroelastic interactions need to be examined in very light aircraft. Very light aircraft (VLA) are specified as single-engine air vehicles with a maximum take-off weight of not more than 750 kg, having one or two seats [1]. Turkish Aerospace Industry (TAI) and Middle East Technical University (METU) have collaborated to design and develop a very light category aircraft. In this project, it is aimed that METU students carry out a real aircraft design process under the supervision of METU professors and with the support of TAI personnel. METU VLA project has started in March 2018 and been proceeding with the contributions of students and faculty members from the aerospace, mechanical, electrical, industrial engineering and industrial design departments. In this context, the low wing configuration with a conventional tail and two side-by-side seats is chosen. Table 1.1 gives the general specifications of the designed aircraft, which are based on the preliminary design report of the VLA project dated February 2021 [7].

The relevant certification regulation CS-VLA [1] requires that the aircraft is free from flutter, divergence, control surface reversal within the operational envelope. Flight envelope or V-n diagram represents all the possible combinations of airspeed and load factors resulting from maneuver and gust encounter. Load factor is defined in [1] as the ratio of the aerodynamic force component acting normal to the assumed longitudinal axis of the airplane to the weight of the airplane. Figure 1.1 shows the limit

Table 1.1: General specifications of the VLA

Maximum Weight	708 kg
Length of the Airplane	6.04 m
Wing Area	12.74 m^2
Wing Span	9.84 m
Wing Aspect Ratio	7.6

maneuver, gust and combined envelopes in dashed, dot-dashed and solid lines, respectively. V_S, V_A, V_C and V_D appeared on the diagram are design airspeeds and they correspond to stalling speed, design maneuvering, cruising and dive speeds, sequentially. The leftmost-hand corners of the maneuver envelope are shaped by the stalling characteristics of the aircraft, whereas the right-hand corners are determined by the maximum speed states of the aircraft [3]. The horizontal lines at the upper and lower boundaries of the maneuvering envelope correspond to the positive and negative limit maneuvering load factors. On the other hand, the gust envelope is obtained by calculating the gust load factor for positive and negative gust conditions encountered at cruise and dive speeds and then linearly combining these points with the positive 1g load factor point located on the vertical axis. Gust condition can be critical for light aircraft, as significant acceleration can be seen due to low inertial resistance [8], which can result in a load factor even greater than the limit maneuvering load factor. The combined envelope covers all the possible load cases coming from maneuvering or atmospheric gust.

Design airspeeds and limit maneuvering load factors of the VLA in question in this study are given in Table 1.2.

Starting from the early phases of aircraft design processes, flight loads are highly demanded data and valuable input for structural design. However, it can be challenging to obtain the flight loads with complex methods at the early design phases when the project is still immature. In this work, distributed flight loads are obtained and the aeroelastic stability characteristics are estimated using MSC.Nastran and MSC.FlightLoads. The motivation of the thesis is to present a practice on aeroelastic analysis of a full aircraft model by covering the static aeroelastic, flutter and

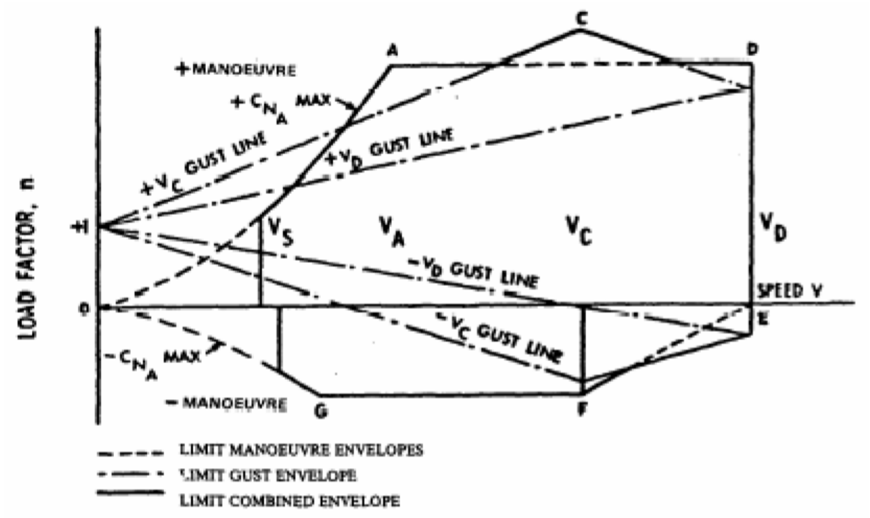

Figure 1.1: Flight envelope, from [1]

Table 1.2: Design speeds and limit load factor of the VLA

Stall Speed, V_S	48.9 KIAS
Design Maneuver Speed, V_A	95.4 KIAS
Design Cruise Speed, V_C	110 KIAS
Design Dive Speed, V_D	137.5 KIAS
Positive Manoeuvring Limit Load Factor	3.8 g
Negative Manoeuvring Limit Load Factor	-1.5 g

gust response aspects. Another driving force behind this study is the inquiry about if we can benefit more from the commercial tool in hand by developing different modeling approaches and reduce the dependency on higher-order aerodynamic solutions for structural purposes.

For the studies carried out within the scope of this thesis, ideas are adopted from various publications in the literature summarized below.

In [9], the structural layout, materials used, and finite element model of a twin wing-tail boom configuration unmanned air vehicle is described, and detailed aeroelastic stability analyses are conducted. They add one sub-structure at a time to see the effect of each sub-structure on the critical aeroelastic stability modes and speeds. Aerodynamic modeling of the fuselage is also discussed in this study. Furthermore, the structural and aerodynamic mesh refinement effect is also covered. Finally, different aero-structure coupling methods and choice of interpolation points are discussed.

[8] analyses a concept, unmanned aircraft by conducting static aeroelastic, flutter and 1D discrete gust analysis using MSC.Nastran. Most of all, a tuned discrete gust approach described in [10] with various gust gradient lengths is adopted. Gust gradient length is the distance over which the gust velocity increases to the maximum value. In this approach, gust velocities are tuned for different gust gradient lengths. The results were such that critical responses for different types of loadings do not come from a single gust gradient length but from a range of length.

DLM is the aerodynamic theory employed in Nastran for subsonic flows. The theory is presented in 1969 by Albano and Rodden [11], in 1971 and 1972 by Giesing, Kalman and Rodden [12, 13, 14, 15]. The theory of the DLM is based on linearized aerodynamic potential theory. The undisturbed flow is uniform and it can be steady or harmonically varying. DLM is an extended version of the steady Vortex-Lattice method for unsteady flows. It assumes all lifting surfaces lying parallel to the flow and does not allow for modeling the angle of incidence, camber or twist while creating the aerodynamic mesh. There are studies applying initial downwash input to include initial incidence or camber distribution over the lifting surfaces. In [16], both the camber and incidence of the wing are included, and Figure 1.2 shows their comparison of the local lift coefficient of the wing with and without this correction.

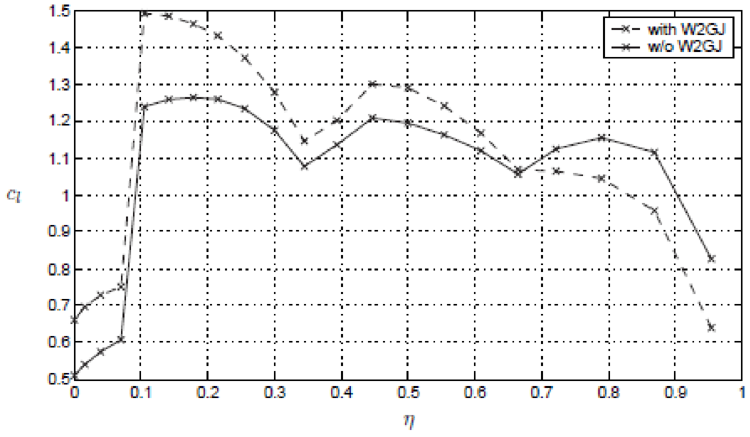

Figure 1.2: Local lift coefficient of the wing with and without DLM correction, from [16]

Dillinger et al. conclude in [17] that pressure distributions computed with corrected DLM and higher-order aerodynamics show good agreement. However, this only holds for lower, recompression shock-free Mach numbers. Figure 1.3 demonstrates the comparison of the pressure difference between the upper and lower surfaces for camber-corrected DLM and the higher-order aerodynamic computational fluid dynamics (CFD) method TAU.

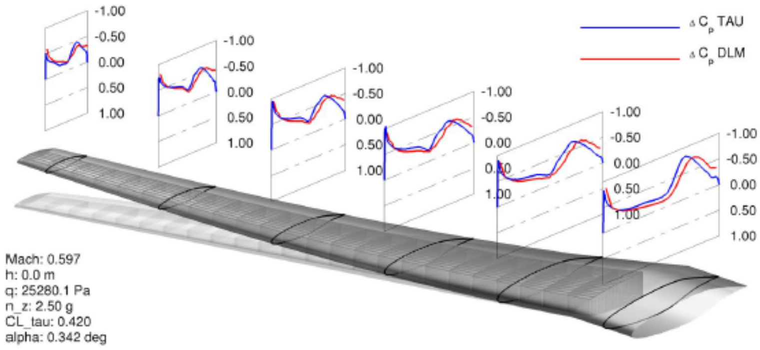

Figure 1.3: Comparison of camber-corrected DLM and higher-order aerodynamic method TAU, from [17]

A couple of test case studies are conducted to practice the static and dynamic aeroelastic analysis methods used in the thesis. The articles given below are utilized to verify the obtained results.

In 1963, Yates [18] presented measured modal frequency and flutter results for several configurations of the AGARD wing obtained from wind tunnel experiments at various conditions. In 1987, Yates [19] published the computational modal frequencies using the finite element method and plotted the mode shapes of the AGARD 445.6 wing. Kolonay presents in his Ph.D. thesis [20] an unsteady aerodynamic analysis example by using the AGARD 445.6 wing. In [20], first, the material properties are tuned in order to match the mode shapes and frequencies given in [19], where the model masses are also consistent.

For the static aeroelastic analysis of the AGARD wing, Cai and Liu used a coupled computational fluid dynamics and computational structural dynamics method in [21]. Chordwise pressure coefficient distributions are presented for rigid and elastic wing cases in addition to the spanwise variations of the wing twist and the vertical deflection at the leading and trailing edges.

Lastly, the gust response of the AGARD wing is studied by Förster and Breitsamter [22]. They compare two different approaches developed to predict loads due to discrete gust. For 1-cosine gust excitation, the responses of the generalized modal coordinates obtained by employing nonlinear time domain and small disturbance frequency domain approaches are given.

In this thesis study, static and dynamic aeroelastic characteristics of the VLA designed within the scope of the METU-VLA project are investigated. The global finite element model of the VLA project is utilized as the structural model for aeroelastic analysis. By using MSC.FlightLoads and Dynamics, the aeroelastic model is generated. Aerodynamic calculations are based on the Doublet-Lattice Method (DLM), which is a panel method applicable to subsonic, unsteady flows. Aeroelastic model is obtained by coupling the aerodynamic and structural models. Flexible trim, flutter and discrete gust response analysis are conducted.

Further discussions cover improvement of the aerodynamic solution, aerodynamic modeling approaches and aero-structure coupling alternatives. The aerodynamic solution is improved by including the camber and the angle of incidence of the wing through the addition of an initial downwash into the initial DLM solution. DLM-based loads are compared with loads obtained from computational fluid dynamics (CFD) analysis. Additionally, different aerodynamic modeling approaches are implemented in the analysis. These models differ from each other in terms of handling the gap between wing aerodynamic panels. The effects of aeroelastic model corrections on static trim, flutter and gust response solutions are investigated.

The organization of the thesis is as follows. In Chapter 2, the structural and aerodynamic models and their coupling are explained in detail. Chapter 3 covers the theory of the aeroelastic analysis methods employed in Nastran. Test case studies conducted with the AGARD wing are shown in Chapter 4. Next, in Chapter 5, aeroelastic analyses results of the VLA are presented and discussed. Finally, concluding remarks and future work are given in Chapter 6.

CHAPTER 2

AEROELASTIC MODEL DESCRIPTION

This chapter covers the aeroelastic modeling of the VLA. The aeroelastic model is generated by coupling the structural and aerodynamic models. Details of the structural and aerodynamic models are given and the coupling method is explained. Additionally, the improvement of the aerodynamic solution is presented here.

MSC Flight Loads and Dynamics Module and NASTRAN solvers are used in modeling and analysis. Figure 2.1 demonstrates the flight-loads module architecture. It is capable of defining the aerodynamic and structural models, performing aerodynamic calculations, analyzing the combined aero-structure model, displaying the results and post-processing.

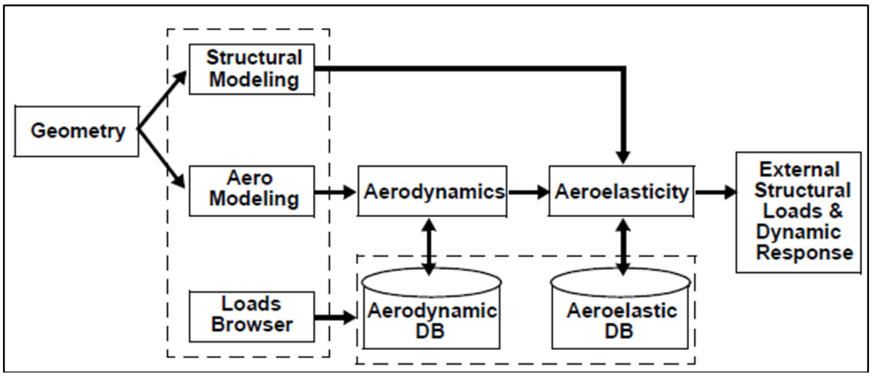

Figure 2.1: Architecture of MSC.FlightLoads Module, from [23]

2.1 Structural Model

The structural model is the global finite element model of the whole aircraft, as shown in Figure 2.2. The finite element model used in this study is the version dated March 2021.

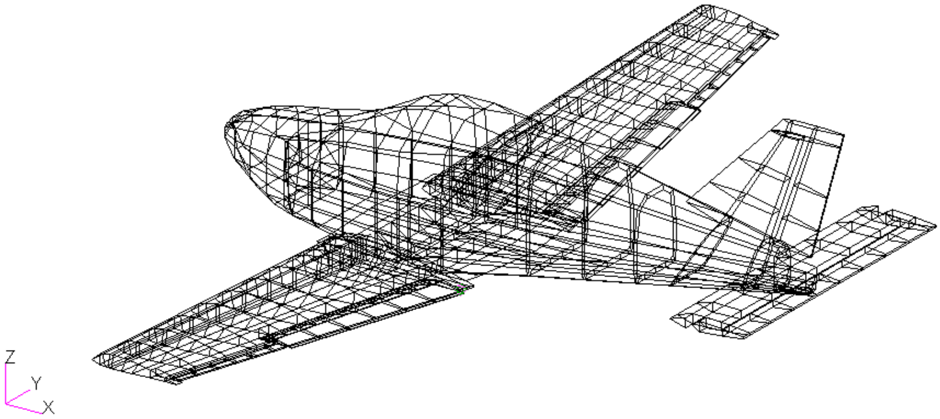

Figure 2.2: Structural finite element model

The VLA has a metallic airframe and structural components are made of different types of aluminum. In the structural model, linear elastic, isotropic material properties are assigned to elements. The model consists of 1439 1-D linear elements and 1693 2-D shell elements. One-dimensional elements are used to model stringers, flanges, longerons where spar webs, ribs and skin structures are modeled by triangular or quadrilateral shell elements. Besides the structural mass, concentrated mass elements are utilized to represent the mass distribution, including the instruments, payload, equipment, fuel, etc. After all, the model used in the analysis has a mass of 715 kg.

Control surfaces are modeled by using multi-point constraints (MPCs) between the coincident nodes, where one of the coincident nodes is connected to the main surface and the other is to the control surface. Local coordinate systems are defined such that one of the coordinate axes is aligned with the hinge line. MPCs connecting the main surfaces and control surfaces allow the rotation about the hinge axes. In order to represent the actuator stiffness, torsional springs are modeled by CBUSH elements created between the two coincident nodes. Spring constants in the direction of rotation about the hinge axis are determined by trial and error in such a way that control surface deflection modes appear in modal analysis without coupling with the motion of other parts of the aircraft. Control surfaces rotate freely at very low frequencies when too low stiffness input is given. Starting with the low stiffness values, motion at the control surface rotation modes is observed as the stiffness values are increased. After some point, when the stiffness of a surface is further increased, that surface does not rotate on its own, but the other parts of the structure get involved in the mode shape. The rotational stiffnesses of the CBUSH elements are not increased up to that level. Hence, control surface stiffnesses are determined so that control surface deflection modes appear without coupling with the motion of other parts of the structure.

The frequencies of the control surface modes are compared to similar airplanes' corresponding modal frequencies to check if determined stiffness values give reasonable results. [24] presents mode shapes and modal frequencies of FM-250 "Vampire II" obtained by ground vibration tests and [25] lists normal modes and normal frequencies of LASTA aircraft through computational modal analysis. LASTA is an aerobatic military trainer aircraft with the maximum take-off weight (MTOW) of 1210 kg, where FM-250 "Vampire II" is an ultralight sport aircraft with 600 kg MTOW. The VLA is considered to be somewhere in between the referred airplanes in terms of classification. Furthermore, the first bending modal frequencies of the VLA, LASTA aircraft and FM-250 "Vampire II" are similar. Therefore, the natural frequencies of control surface rotational modes of these aircraft can give an idea for this study. Comparison of control surface modal frequencies is given in Table 2.1, along with the first wing bending frequencies. Control surface modeling with assumed stiffness values appears to result in reasonable frequencies, considering those of similar aircraft.

In static aeroelastic and gust response analysis, the symmetric boundary condition is applied at the center of gravity of the aircraft model. CG location of the finite element model is obtained by executing the grid point weight generator of Nastran. A node is created at the detected CG location and it is connected to the structural model with RBE2 rigid body elements. Two nodes are selected from each of the front and rear wing spars inside the fuselage for RBE2 connection, as shown in Figure 2.3. These nodes are dependent on the CG node in all degrees of freedom. Finally, single point

Table 2.1: Comparison of modal frequencies of the VLA with the referred aircraft

Modes	VLA	LASTA	FM-250
1^{st} wing bend.	10.056 Hz	11.397 Hz	8.575 Hz
Rudder rot.	7.328 Hz	7.316 Hz	6.941 Hz
Elevator rot.	8.171 Hz	8.140 Hz	15.06 Hz
Aileron rot.	15.368 Hz (sym)	14.596 Hz (sym)	-
	15.139 Hz (antisym)	-	14.630 Hz (antisym)
Flap rot.	20.105 Hz (sym)	24.759 Hz (sym)	-
	20.568 Hz (antisym)	24.367 Hz (antisym)	-

constraint is applied to CG in translation in x and y directions and rotation about x and z directions (see Figure 2.2 for the coordinate system).

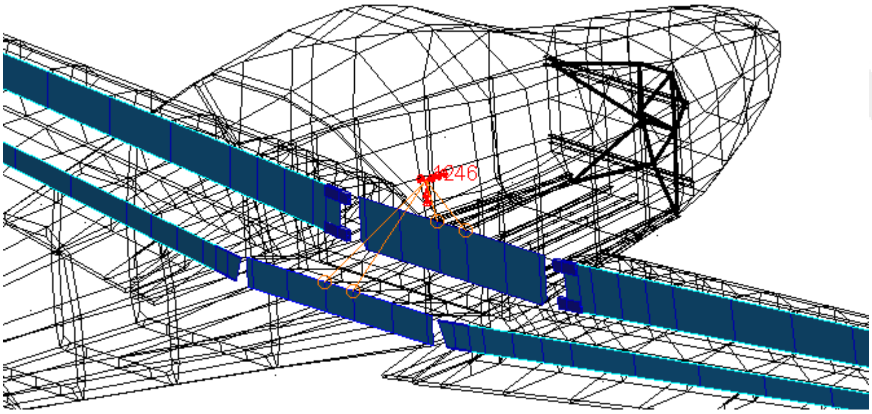

Figure 2.3: Connection of the CG node to the structure

2.2 Aerodynamic Model

The aerodynamic model of this study covers flat plate aero modeling of lifting surfaces. Wings, horizontal and vertical tails, and control surfaces are defined as lifting surfaces and aerodynamic boxes are created by meshing the predefined lifting surfaces. It is recommended to concentrate aerodynamic boxes near the leading edge, trailing edge and hinge lines [26]. Therefore, both uniformly distributed and biased meshing is used in order to increase mesh concentration at the critical regions. Considering the model quality, aspect ratios of the individual aerodynamic boxes are preferred to be approximately unity and less than three is acceptable for subsonic flow [26]. In this case, the aerodynamic mesh is created by taking this point into consideration and it is checked that the aspect ratio of each element does not exceed three. The fuselage is not modeled as an aerodynamic body in this study. However, in the absence of the fuselage, the gap between the wing surfaces results in unrealistic vortices at the inboard wing region [27]. Therefore, wing panels are extended to cover the gap between the wings to obtain a more accurate pressure distribution over the wings. A similar approach is presented in [9] and the effect of bridging the gap between the wings on flutter results is discussed.

Figure 2.4 shows the aerodynamic mesh with and without the wing bridging panels. The mesh shown in Figure 2.4a consists of 1448 aerodynamic elements, whereas there are 1604 elements in Figure 2.4b.

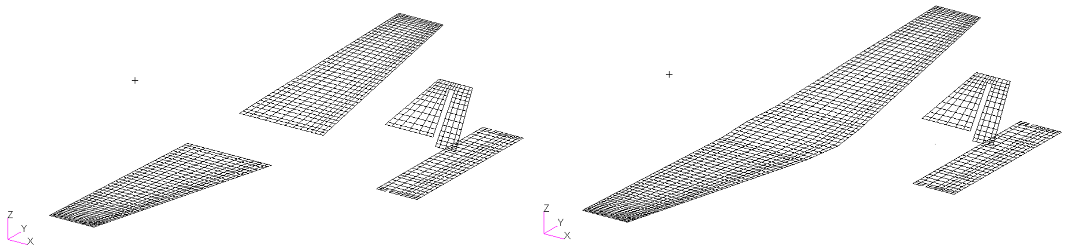

(a) Without wing bridging panels

(b) With wing bridging panels

Figure 2.4: Aerodynamic models

Lifting surfaces corresponding to ailerons, flaps, elevator, and rudder are assigned as control surfaces. Control surface hinge axes are specified and the angular position limits are provided for each control surface in accordance with the design. Operational limits for the rudder and aileron are ±30°, for the elevator it is ±25°, and the maximum flap deflection is 30°.

2.2.1 Aerodynamic Theory

Doublet-Lattice aerodynamics is provided in MSC.Nastran for subsonic flows. DLM is a panel method in which lifting surfaces are represented by flat panels and the panels are assumed to be parallel to the flow. Aerodynamic forces are calculated over the aerodynamic elements. DLM requires these elements to be trapezoidal boxes with sides parallel to the air-stream. For Doublet-Lattice forces, the surface normalwash boundary condition is satisfied at 75% chordwise station and spanwise center of the box while the unknown lifting pressures are assumed to be concentrated uniformly across the 25% chord line of each box [26].

In order to account for the effects of the wing incidence angle and camber, initial downwash is dictated as input on Direct Matrix Input (DMI) entries of Nastran. To include the camber effect, the initial angle of attack of each aerodynamic box is calculated at the collocation point, which is located at the 75% chord location of the boxes. The slope of each aerodynamic element is calculated from the mean camber line equation of the wing profile and it is added to the wing incidence angle, which is constant for all wing elements. The VLA wing does not have a varying twist through the span. Therefore, to account for the wing incidence effect, all aerodynamic boxes are rotated by the same angle, which is 2.0°. Fig. 2.5 representatively shows the local angles of attack given to aerodynamic elements for camber and incidence corrections.

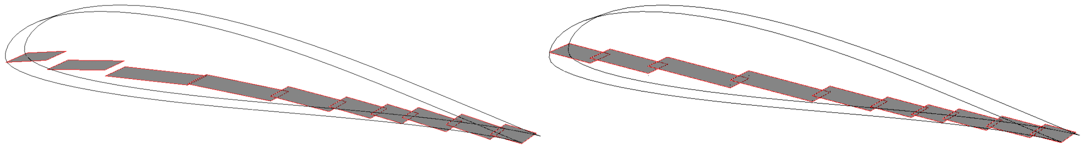

(a) Camber

(b) Incidence

Figure 2.5: DLM correction for a chordwise strip of aerodynamic boxes

Airfoil SD7062 with the maximum camber of 3.5% at 38.8% chordwise location is used in the VLA wings. A camber line equation is not provided for SD7062 airfoil. Here, as a starting point, the points on the camber line are assumed to be equidistant to the points on the upper and lower surfaces at the same chordwise location. The mid-points of the upper and lower surfaces are given in Figure 2.6 as camber data and shown with dark red markers. A curve is fitted to these data points and the equation of the curve is used to find the slope at certain points. However, this is not the proper definition of the mean camber line of an airfoil. [28] shows that the mid-point of the normal to the chord line at any location along the airfoil does not necessarily lie on the camber line. A geometric approach is also described in [28] for constructing the camber lines of arbitrary airfoils.

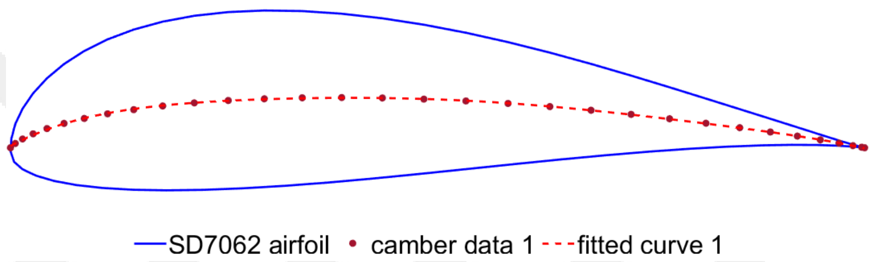

Figure 2.6: SD7062 airfoil and the first estimation of the camber line

In our case, the accuracy of the first camber line estimation is checked at certain points by applying the following procedure. Tangent lines are drawn to the assumed camber line on certain points denoted by C_i in Figure 2.7, where i refers to the chordwise stations and takes the values between 1 to 7. Derivative of the fitted equation is used to describe the tangent lines. Then, perpendicular secants are drawn to tangent lines, and the intersection of a secant with upper and lower surfaces are indicated as A_i and B_i.

For a properly defined mean camber, the points on the camber line C_i, should be equidistant to A_i and B_i. The distances, $|A_iC_i|$ and $|B_iC_i|$, are listed in Table 2.2 and the errors are given in percent. Table 2.2 demonstrates that assuming the camber line as the mid-surface of the airfoil, which is referred to as the 1^{st} estimation in the table, leads to high errors around the leading edge. Therefore, the locations of the points around the leading edge are updated so that the new C_i points lie on the center

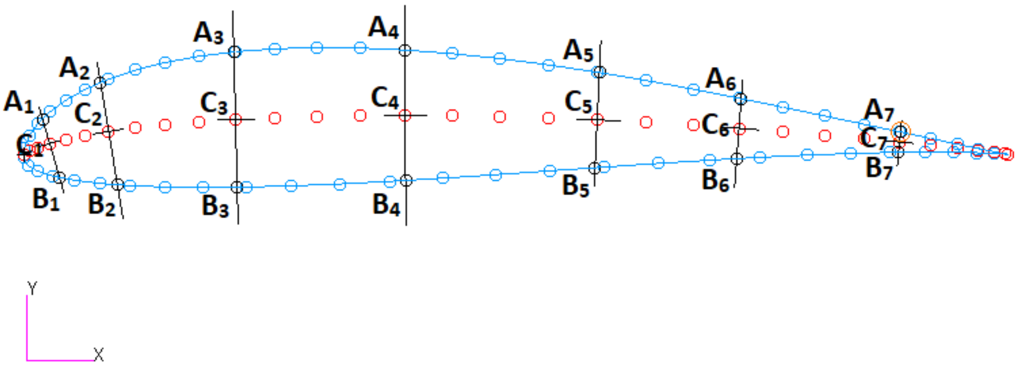

Figure 2.7: Geometric examination of the initially estimated camber

of $|A_iB_i|$ lines, and a new curve is fitted to the updated data points. In Figure 2.8 the second estimation of the camber line is shown together with the first one. The controlling procedure of the geometric constraint of the mean camber line definition is repeated for the second set of camber data by utilizing the newly fitted equation, and the results are given in Table 2.2 under the 2nd estimation title.

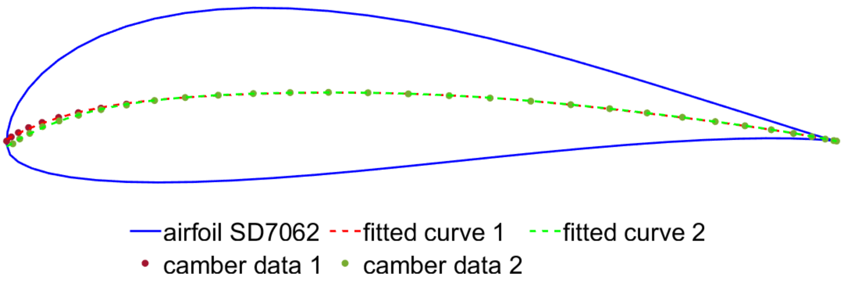

Figure 2.8: The 1st and the 2nd estimations of the mean camber

Table 2.2 reveals that the second estimation of the camber is a more accurate representation. Therefore the mean camber line equation for the unit chord length airfoil is assumed as

$$\begin{aligned} y = & -1.3405x^6 + 4.6386x^5 - 6.3904x^4 + 4.5008x^3 \\ & -1.8301x^2 + 0.426x - 0.0045 \end{aligned} \tag{2.1}$$

where x is the chordwise location. Eq. 2.1 gives the 2nd fitted curve in Figure 2.8.

Table 2.2: Comparison of the 1st and the 2nd approximations of the mean camber

	1st Estimation			2nd Estimation		
Chordwise station i	**$\mathbf{|A_iC_i|}$ [mm]**	**$\mathbf{|B_iC_i|}$ [mm]**	**error [%]**	**$\mathbf{|A_iC_i|}$ [mm]**	**$\mathbf{|B_iC_i|}$ [mm]**	**error [%]**
1	0.02592	0.03577	15.95	0.03021	0.03154	2.15
2	0.05042	0.05472	4.09	0.05221	0.05296	0.71
3	0.06863	0.06883	0.15	0.06845	0.06890	0.32
4	0.06623	0.06622	0.01	0.06623	0.06623	0.00
5	0.04813	0.04868	0.56	0.04814	0.04867	0.55
6	0.03026	0.03086	0.98	0.03026	0.03085	0.97
7	0.01028	0.01051	1.09	0.01028	0.01004	1.16

2.3 Aeroelastic Coupling

The coupling between the aerodynamic and structural meshes is established by splining. Splining is an interpolation method connecting the structural and aerodynamic grids. The structural degrees of freedom (DOFs) are the independent ones, whereas the aerodynamic DOFs are dependent. An interpolation matrix is used, which relates the deflections of structural grids to the deflections of aerodynamic grids [26].

$$\{u_k\} = [G_{kg}]\{u_g\} \tag{2.2}$$

where subscripts k and g denotes the aerodynamic and structural grid sets, respectively.

Yet, one more transformation is required, which conducts a relationship between the aerodynamic forces and the structural forces acting on the structural grids. There is structural equivalence in these force systems, meaning that the aerodynamic and structural forces deflect the structure equally. Therefore the aerodynamic forces $\{F_k\}$ and structural forces $\{F_g\}$ do the same virtual work [26].

$$\{\delta u_k\}^T\{F_k\} = \{\delta u_g\}^T\{F_g\} \tag{2.3}$$

where $\{\delta u_k\}$ and $\{\delta u_k\}$ are virtual deflections.

Substituting Eq. (2.2) into Eq. (2.3) and rearranging yields

$$\{\delta u_g\}^T([G_{kg}]^T\{F_k\} - \{F_g\}) = 0 \tag{2.4}$$

Hence, the required force transformation is found as:

$$\{F_g\} = [G_{kg}]^T\{F_k\} \tag{2.5}$$

Various methods are available in MSC.Nastran for linear and surface spline types. In this study, the Infinite Plate Spline (IPS) interpolation method is used to couple aerodynamic and structural models. IPS is a widely preferred option among spline types available in Nastran, and it is suitable for wing-like components [29]. The displacement mapping procedure of IPS can be illustrated as in Figure 2.9 and explained as follows [30]:

- Structural grids in their undeformed positions are projected from a finite element modal on an infinite plate with fixed edges at infinity. (See Figures 2.9a and 2.9b)
- Grids are perturbed normal to the infinite plate by their displacements. (See Figure 2.9c)
- By using these perturbed displacements as boundary conditions, the infinite plate is fit to these displaced grids. (See Figure 2.9d)
- Then, the aero mesh grids are placed on the infinite plate. (See Figure 2.9e)
- Now, the aero mesh can deform by following the displacements of the infinite plate. (See Figure 2.9f)

All the structural nodes located on the upper skins of lifting surfaces are selected for the transformation. Moreover, the effects of splining the wing bridging panels and the fuselage structure on the aeroelastic solutions are discussed in Chapter 5. For aeroelastic coupling of the bridge, the structural nodes are selected from the front and rear spars passing through the fuselage. In Fig. 2.10, the structural model is shown in black, where the blue mesh represents the lifting surface connecting the left and right wings and red markers show the structural nodes selected for force and displacement transformation between aerodynamic and structural models.

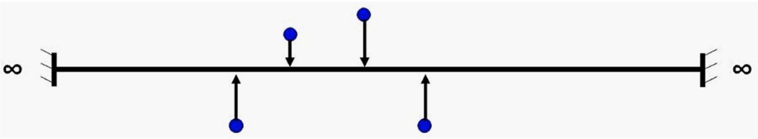

(a) Structural grids in their undeformed position

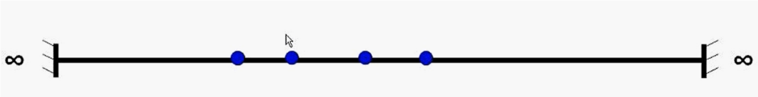

(b) Structural grids projected on the infinite plate

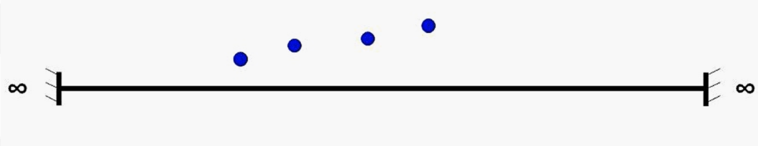

(c) Perturbed structural grids

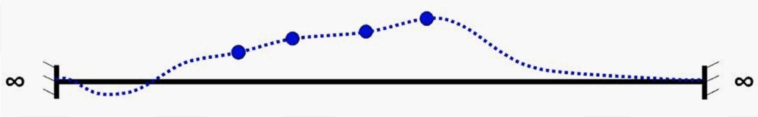

(d) Displacement of the infinite plate

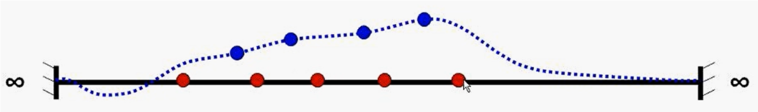

(e) Aerodynamic grids on the infinite plate

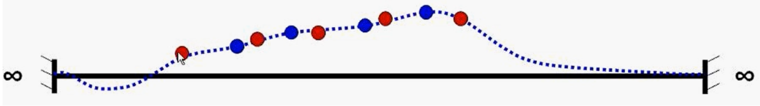

(f) Displacement of aerodynamic grids

Figure 2.9: Illustration of how IPS works, from [30]

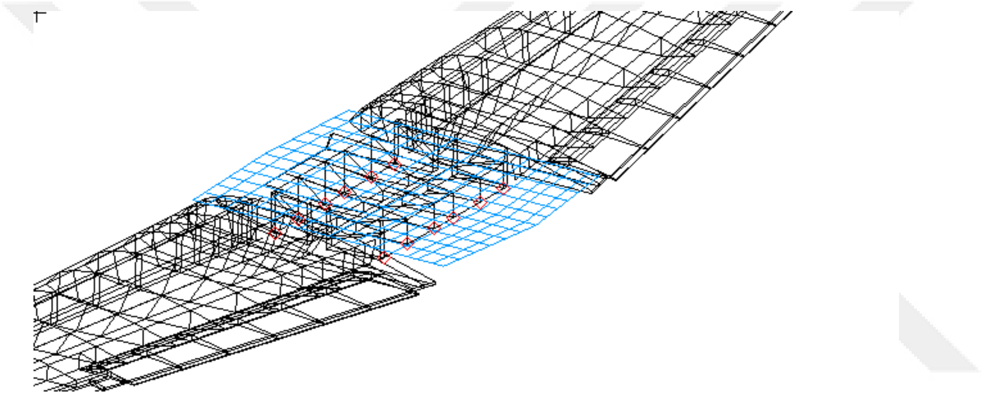

Figure 2.10: Structural grid selection for coupling the wing bridging plate and the structure

CHAPTER 3

THEORY

This chapter covers the static aeroelasticity, flutter and dynamic response equations of motion. First, the trim solution of MSC.Nastran is introduced. Next, the dynamic stability equation is derived and the fundamentals of the PK method, which is employed in the flutter analysis of the thesis, are given. Lastly, the aeroelastic response solution approach of Nastran is explained.

3.1 Static Aeroelasticity

The static aeroelastic analysis aims to determine the loads on the aircraft due to stationary or quasi-stationary maneuvers. A set of trim parameters are specified to describe the maneuver. A subset of the trim parameters is defined by the user and the remaining trim parameters are determined during the analysis.

The equations of motion obtained by putting the aircraft into steady state load equilibrium is given and manipulated in Chapter 2.5 of [26]:

$$[M_{aa}]\{\ddot{u}_a\} + [K_{aa} - \bar{q}Q_{aa}]\{u_a\} = \bar{q}[Q_{ax}]\{u_x\} + \{P_a\} \tag{3.1}$$

where $[M_{aa}]$ is the structural mass matrix, $[K_{aa}]$ is the structural stiffness matrix and $\{P_a\}$ is the vector of applied loads. The aerodynamic degrees of freedom $\{u_a\}$ and $\{u_x\}$ in Eq. (3.1) indicate the structural analysis set and aerodynamic extra points, or vector of controllers. Aerodynamic extra points are used to describe control surface deflections and overall rigid body motions. $\bar{q}$ symbolizes the flight dynamic pressure. $\bar{q}[Q_{aa}]$ refers to the aerodynamic influence coefficient matrix that provides the forces at the structural grip points due to structural deformations, where $\bar{q}[Q_{ax}]$ gives the rigid aerodynamic forces at the structural grid points due to unit deflections of the aerodynamic extra points. Aerodynamic loads are a function of the elastic deformations, the aerodynamic angles, the rotational rates and the deflections of the control surfaces.

MSC.Nastran requires the user to identify unrestrained rigid-body degrees of freedom to represent the free-flying characteristic of the aircraft. Quantities referring to these reference (support) DOF are denoted by subscript r, whereas the ones referring to the leftover DOF are denoted by subscript l. The leftover degrees of freedom describe the aeroelastic response within the support frame [31]. Eq. (3.1) can be partitioned into $r - set$ and $l - set$ DOF as:

$$\begin{bmatrix} {K_{ll}}^a & {K_{lr}}^a \\ {K_{rl}}^a & {K_{rr}}^a \end{bmatrix} \begin{Bmatrix} u_l \\ u_r \end{Bmatrix} + \begin{bmatrix} M_{ll} & M_{lr} \\ M_{rl} & M_{rr} \end{bmatrix} \begin{Bmatrix} \ddot{u}_l \\ \ddot{u}_r \end{Bmatrix} = - \begin{bmatrix} {K_{lx}}^a \\ {K_{rx}}^a \end{bmatrix} \begin{Bmatrix} u_x \end{Bmatrix} + \begin{Bmatrix} P_l \\ P_r \end{Bmatrix} \tag{3.2}$$

where

$${K_{aa}}^a = [K_{aa} - \bar{q}Q_{aa}] \quad \& \quad {K_{ax}}^a = -\bar{q}[Q_{ax}].$$

The rigid body mode matrix is introduced as:

$$D = -[K_{ll}]^{-1}[K_{lr}]. \tag{3.3}$$

Multiplying the first row of Eq. (3.2) by D^T and adding to the second row yields

$$\begin{aligned} &\begin{bmatrix} {K_{ll}}^a & {K_{lr}}^a \\ D^T K_{ll} + {K_{rl}}^a & D^T K_{lr} + {K_{rr}}^a \end{bmatrix} \begin{Bmatrix} u_l \\ u_r \end{Bmatrix} \\ + &\begin{bmatrix} M_{ll} & M_{lr} \\ D^T M_{ll} + M_{rl} & D^T M_{lr} + M_{rr} \end{bmatrix} \begin{Bmatrix} \ddot{u}_l \\ \ddot{u}_r \end{Bmatrix} \\ = - &\begin{bmatrix} {K_{lx}}^a \\ D^T {K_{lx}}^a + {K_{rx}}^a \end{bmatrix} \begin{Bmatrix} u_x \end{Bmatrix} + \begin{Bmatrix} P_l \\ D^T P_l + P_r \end{Bmatrix}. \end{aligned} \tag{3.4}$$

Two relations are given in [26] for the undetermined accelerations $\ddot{u}_l$ and $\ddot{u}_r$. The first relation is based on the assumption of quasi steady equilibrium and given as:

$$\{\ddot{u}_l\} = D\{\ddot{u}_r\} \tag{3.5}$$

where $[D]$ is the rigid body matrix given in Eq. (3.3). By implementing the relation of Eq. (3.5), Eq. (3.4) reads

$$\begin{bmatrix} K_{ll}{}^{a} & K_{lr}{}^{a} \\ D^T K_{ll} + K_{rl}{}^{a} & D^T K_{lr} + K_{rr}{}^{a} \end{bmatrix} \begin{Bmatrix} u_l \\ u_r \end{Bmatrix} + \left[\begin{array}{cc} M_{ll} D & M_{lr} \\ \multicolumn{2}{c}{m_r} \end{array} \right] \begin{Bmatrix} \ddot{u}_r \end{Bmatrix}$$
$$= - \begin{bmatrix} K_{lx}{}^{a} \\ D^T K_{lx}{}^{a} + K_{rx}{}^{a} \end{bmatrix} \begin{Bmatrix} u_x \end{Bmatrix} + \begin{Bmatrix} P_l \\ D^T P_l + P_r \end{Bmatrix} \quad (3.6)$$

where $[m_r] = [D^T M_{ll} D + M_{rl} D + D^T M_{lr} + M_{rr}]$. The second relation associates the $\{\ddot{u}_r\}$ with the aerodynamic extra points $\{u_x\}$ by the following expression

$$\{\ddot{u}_r\} = [TR]^T [TRX] \{u_x\}. \quad (3.7)$$

$[TRX]$ in Eq. (3.7) extracts the rigid body accelerations from the set of trim parameters $\{u_x\}$, and $[TR]^T$ transforms accelerations from the aerodynamic reference point to the supported degrees of freedom.

In the most general case, the vector of trim parameters $\{u_x\}$ involves the angle of attack α; the angle of sideslip β; the roll, pitch and yaw velocities p, q, r; two linear acceleration components a_2 and a_3; three angular acceleration components $\dot{p}$, $\dot{q}$, $\dot{r}$; and the aileron, elevator and rudder control surface rotations δ_a, δ_e, δ_r,

$$\{u_x\} = \{\alpha, \beta, p, q, r, a_2, a_3, \dot{p}, \dot{q}, \dot{r}, \delta_a, \delta_e, \delta_r\}. \quad (3.8)$$

The longitudinal acceleration and thrust input is not considered. Therefore, five acceleration components, the linear accelerations in lateral and vertical directions and rotational accelerations in all 3 directions, are given in Eq. (3.8).

3.2 Dynamic Aeroelastic Stability

The flutter equation is derived in this section and the pk-method of flutter solution is explained.

First, a trimmed reference state is considered. The equation of the motion for an air vehicle reads [32]:

$$[M]\{\ddot{u}_a^s\} + [K]\{u_a^s\} = \{p_a^s\} + [A_a^s(u_a^s, u_x)] \quad (3.9)$$

where $[M]$ is the mass matrix, $[K]$ is the stiffness matrix and $A_a^s(u_a^s, u_x)$ is the aerodynamic loads matrix which is a function of structural displacements $\{u_a^s\}$ and the trim parameters u_x. In addition, $\{p_a^s\}$ vector represents the external forces.

Then, a small time dependent disturbance $\{p_a(t)\}$ is applied. Small additional disturbance $\{u_a(t)\}$ is induced due to small disturbance. Eq. (3.9) should be satisfied with the total displacement of $\{u_a^s + u_a(t)\}$

$$\begin{aligned}[M]\{\ddot{u}_a^s + \ddot{u}_a(t)\} + [C]\{\dot{u}_a(t)\} + [K]\{u_a^s + u_a(t)\} \\ = \{p_a^s + p_a(t)\} + [A_a^s(u_a^s + u_a(t), u_x)]\end{aligned} \tag{3.10}$$

where $[C]$ is the structural damping matrix.

The aerodynamic forces are linearized with respect to $\{u_a(t)\}$ which disturbs the reference state. In Eq. (3.11), the first term on the right-hand side represents the aerodynamic forces before the disturbance, whereas the convolution integral in the second term gives the aerodynamic forces due to disturbance.

$$[A_a^s(u_a^s + u_a(t), u_x)] = [A_a^s(u_a^s, u_x)] + \int_0^t a_{aa}(u_a^s, u_x, t-\tau)\{u_a(\tau)\}\, d\tau \tag{3.11}$$

By substituting the Eq. (3.11) and assuming that the small time dependent force $p_a(t)$ is equal to zero at $t > 0$, the Eq. (3.10) can be written as

$$[M]\{\ddot{u}_a(t)\} + [C]\{\dot{u}_a(t)\} + [K]\{u_a(t)\} = \int_0^t a_{aa}(u_a^s, u_x, t-\tau)\{u_a(\tau)\}\, d\tau \tag{3.12}$$

If the perturbation $u_a(t)$ dies out with increasing time, the system is called stable. If the amplitude of the displacement stays constant in time, then the system is naturally stable. Flutter occurs and the system is called unstable when the $u_a(t)$ increases with increasing time.

In the case of steady harmonic vibrations, the displacement $u_a(t)$ is defined as:

$$\{u_a(t)\} = [U_a(\omega)]e^{i\omega t}. \tag{3.13}$$

Then, the aerodynamic loads become

$$[A_a(t)] = q[Q(M,k)][U_a(\omega)]e^{i\omega t} \tag{3.14}$$

where

$$q[Q(M,k)] = \int_{-\infty}^{\infty} a_{aa}(s)e^{-i\omega s}\, ds\ .$$

In Eq. (3.14), q is the dynamic pressure, $[Q]$ is the aerodynamic force matrix as a function of Mach number and reduced frequency k. Reduced frequency is defined as $k = \frac{\omega\bar{c}}{2V}$, where $\bar{c}$ is the reference chord length.

The dynamic equation for the case of a steady harmonic vibration reads

$$(-\omega^2[M] + i\omega[C] + [K] - q[Q(M,k)])\{U_a\} = [P_a] \qquad (3.15)$$

where the matrix $[P_a]$ in Eq. (3.15) contains the artificial loads needed to sustain the harmonic motion and defined as $[P_a] = -ig[K]\{U_a\}$. g refers to the structural damping coefficient. Substituting the definition of $[P_a]$ into the Eq. (3.15) yields the final form of the flutter equation:

$$(-\omega^2[M] + i\omega[C] + (1+ig)[K] - q[Q(M,k)])\{U_a\} = 0. \qquad (3.16)$$

To find the dynamic stability limit, the values of g for which real roots ω exist are studied as a function of the velocity. If there are real roots for $g > 0$, the system is unstable and flutter occurs. The system is stable if there are no real roots ω for $g > 0$.

The size of the mass and the stiffness matrix in Eq. (3.16) are usually very large since a large number of degrees of freedom are involved in the finite element model of an aircraft structure [29]. Therefore to solve the eigenvalue problem efficiently, modal approach is introduced in which the response of the system is described in terms of a linear combination of the lower order natural modes of the system.

$$\{U_a\} = [\phi]\{U_h\} \qquad (3.17)$$

where $\{U_h\}$ is the generalized coordinates and $[\phi]$ is the modal matrix whose columns contain the lower order natural modes.

Modal reduction is applied by substituting the Eq. (3.17) into the Eq. (3.16), and pre-multiplying with $[\phi]^T$. Flutter equation becomes

$$(-\omega^2[\tilde{M}] + i\omega[\tilde{C}] + (1+ig)[\tilde{K}] - q[\tilde{Q}(M,k)])\{U_h\} = 0 \qquad (3.18)$$

where $[\tilde{M}], [\tilde{C}], [\tilde{K}], [\tilde{Q}]$ are generalized mass, damping, stiffness and aerodynamic force matrices, respectively, and defined as:

$$\begin{aligned}
[\tilde{M}] &= [\phi]^T[M][\phi], \\
[\tilde{C}] &= [\phi]^T[C][\phi], \\
[\tilde{K}] &= [\phi]^T[K][\phi], \\
[\tilde{Q}] &= [\phi]^T[Q][\phi].
\end{aligned}$$

Eq. (3.18) is the reduced general equation of motion of the flutter analyses. Several flutter methods exist to solve this eigenvalue problem. In this study, the PK method is employed in the dynamic stability analysis.

3.2.1 The PK Method of Flutter Solution

The PK method was proposed first by Irwin and Guyett [33] in 1965 and modified by Rodden [34] in 1979. In the modified version of the PK method, the aerodynamic matrix is divided into aerodynamic stiffness and aerodynamic damping matrices.

$$[\tilde{Q}(M,k)] = [\tilde{Q^R}(M,k)] + i[\tilde{Q^I}(M,k)] \tag{3.19}$$

where the real part $[\tilde{Q^R}]$ is the modal aerodynamic stiffness matrix, and the imaginary part $[\tilde{Q^I}]$ is the modal aerodynamic damping matrix.

g is assumed to be zero in the PK method. Therefore, the general flutter equation in generalized coordinates becomes

$$(-\omega^2[\tilde{M}] + i\omega[\tilde{C}] + [\tilde{K}] - q[\tilde{Q}(M,k)])\{U_h\} = 0 \tag{3.20}$$

The eigenvalue p is defined as

$$p = \omega(\gamma \pm i) \tag{3.21}$$

where γ is the transient decay rate coefficient and related to the structural damping coefficient by $g = 2\gamma$.

Note that

$$k = \frac{\omega\bar{c}}{2V} = \frac{Im(p)\bar{c}}{2V}. \tag{3.22}$$

With these relations, the fundamental equation for modal flutter analysis by the PK-method appears as [26]:

$$([\tilde{M}p^2] + ([\tilde{C}] - \frac{1}{4}\frac{\rho\bar{c}V}{k}[\tilde{Q}^I])p + ([\tilde{K}] - \frac{1}{2}\rho V^2[\tilde{Q}^R]))\{U_h\} = 0. \tag{3.23}$$

All the matrices in this eigenvalue problem are real. The PK method computes eigenvalues and eigenvectors for user-specified velocities. An iterative procedure called as reduced frequency "lining-up" process takes place to match the reduced frequency k, with ω, the imaginary part of p. The results of damping are plotted with velocity and the velocity at which damping crosses zero indicates the flutter speed.

3.3 Aeroelastic Response

Different from flutter analysis, the loading term is introduced, which can be either in the frequency domain or in the time domain, in dynamic aeroelastic analysis. For both types of loadings, MSC.Nastran performs all dynamic aeroelastic analyses in the frequency domain [26]. If the user supplies the loading in the time domain, Fourier Transformations are used to convert the loading into the frequency domain, and the outputs of frequency domain analysis are transformed back to the time domain by using Inverse Fourier Transformations.

The basic equation for the aeroelastic frequency response analysis performed in the modal coordinated is as follows [26]:

$$(-\omega^2[\tilde{M}] + i\omega[\tilde{C}] + (1+ig)[\tilde{K}] - \frac{1}{2}\rho V^2[\tilde{Q}(M,k)])\{U_h\} = \{P(\omega)\}. \tag{3.24}$$

The only difference between Eq. (3.24) and Eq. (3.18) is the non-zero right-hand side. $\{P(\omega)\}$ represents the loading in modal coordinates as a function of the analysis frequency.

Eq. (3.25) forms the basis for aeroelastic response analysis.

$$\begin{aligned}\{U_h\} &= [(-\omega^2[\tilde{M}] + i\omega[\tilde{C}] + (1+ig)[\tilde{K}] - \frac{1}{2}\rho V^2[\tilde{Q}(M,k)])]^{-1}\{P(\omega)\} \\ &= [H(i\omega)]\{P(\omega)\}.\end{aligned} \tag{3.25}$$

In this study, transient response analysis is performed by specifying a time-varying gust profile. Discrete "1-cosine" gust profile is defined as [2]:

$$U = \frac{V_g}{2}(1 - cos\frac{2\pi x_g(t)}{L_g}), \quad 0 \leq x_g \leq L_g \tag{3.26}$$

where V_g is gust velocity, L_g is gust length and $x_g(t)$ is the position of the aircraft which is a time dependent parameter.

Fourier transformations are used by MSC.Nastran to convert the load input supplied in the time domain into the frequency domain. Then, the solution performed in the frequency domain provides displacements as a function of frequency. Finally, the responses are turned back into the time domain by inverse Fourier transformations. The Fourier series transformation technique is given as [26]: The circular frequencies are given by

$$\omega_n = 2\pi n\Delta f \quad \text{where} \quad \Delta f = \frac{1}{T}. \tag{3.27}$$

For the time interval of $0 < t < T$, the load transformation for a load at point a is

$$\tilde{P}_a(\omega n) = \int_0^T P_a(t)e^{-i\omega_n t}\,dt\ . \tag{3.28}$$

Eq. (3.29) gives the response at point j

$$\tilde{u}_j(\omega_n) = H_{ja}(\omega_n)\tilde{P}_a(\omega_n) \tag{3.29}$$

Lastly, the response is transformed back to the time domain by

$$u_j(t) = \frac{\Delta\omega}{\pi}[\frac{1}{2}u(0) + \sum_{n=1}^{\infty} Re(\tilde{u}(\omega_n))e^{i\omega_n t}\ . \tag{3.30}$$

CHAPTER 4

TEST CASE STUDY

The aeroelastic analysis methods performed with the VLA model are practiced with a test case, and the analysis results are compared with the results obtained by different methods in the literature. Some of the cases analyzed in this section are transonic even though analyses of the VLA are conducted at subsonic Mach numbers. However, reproducing the results in literature by using the methods of Nastran is the emphasis here. The AGARD wing 445.6 is selected as a test case since it is a standard aeroelastic wing widely studied in the literature. In the 1960s, the AGARD wing was tested in the Transonic Dynamics Tunnel of NASA Langley Research Center to provide an experimental flutter data set as a benchmark for evolving computational methods. Several wing configurations were used in the wind tunnel experiments. In this study, wall-mounted and semi-span "weakened model 3", which is tested in air medium, is considered. The models were constructed of laminated mahogany. The weakened model is obtained by drilling holes through the solid wing, and the holes were filled with foam plastic for the sake of aerodynamic continuity. Planform views of the models used in the test are shown in Figure 4.1.

In this chapter, finite element modeling of the AGARD 445.6 wing is described first. Modal analysis is conducted by MSC.Nastran and calculated modal frequencies are compared with the experimental values to validate the finite element model. Then, the aeroelastic model is introduced. Static aeroelastic, flutter and gust response analysis results of the AGARD wing are compared with the results of other studies in the literature. Experimental flutter data is presented in [18]; however, for the static aeroelastic and gust response cases, computational results in [21] and [22] are referred since experimental results are not readily available.

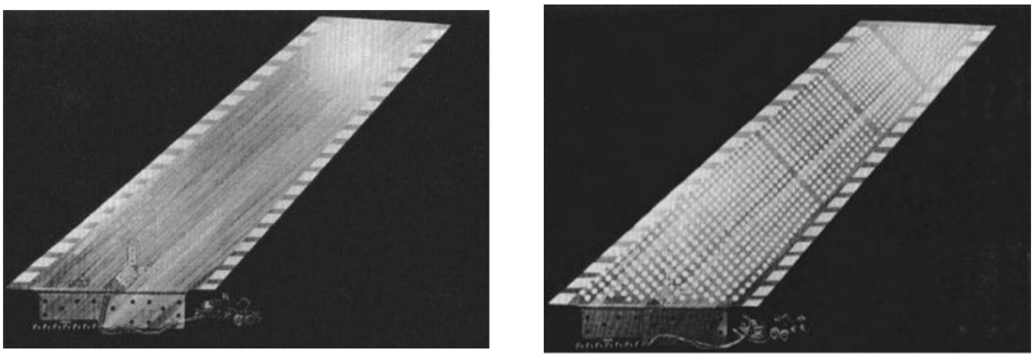

(a) Solid model

(b) Weakened model

Figure 4.1: AGARD 446.5 wing model used in the experiments, from [18]

4.1 AGARD 446.5 Model

The AGARD wing is a tapered, sweptback wing with a symmetrical cross-section. The model has a taper ratio of 0.6576, a panel aspect ratio of 1.6525, a quarter-chord sweptback angle of 45°, and NACA65A004 airfoil section [18]. The wing is modeled as a flat surface. 2-dimensional orthotropic material is assigned to quadrilateral shell elements. The nodes at the wing root are fixed in all degrees of freedom. The structural finite element model and dimensions of the wing can be seen in Figure 4.2. The airfoil shape of the wing cross section is represented by specifying thickness at each node of quadrilateral elements. Figure 4.3 shows the thickness distribution over the wing.

Material properties tuned by Kolonay in [20] are used and listed in Table 4.1. In [19], the higher elastic modulus is said to be along the grain. It is seen from Figure 5.13a that grains of mahogany lie along the span of the wing. Therefore, a local coordinate system is created at the quarter-chord position of the wing root such that one of the axes points out the spanwise direction. Material orientation and directional stiffness properties are specified accordingly by utilizing this coordinate system. Linear elastic, homogeneous material is assigned to the finite elements.

Modal analysis of the weakened AGARD 445.6 wing is conducted by solver 103 of MSC.Nastran. The first four modal frequencies are given in Table 4.2. The frequencies calculated in the current study are compared with the experimental results given

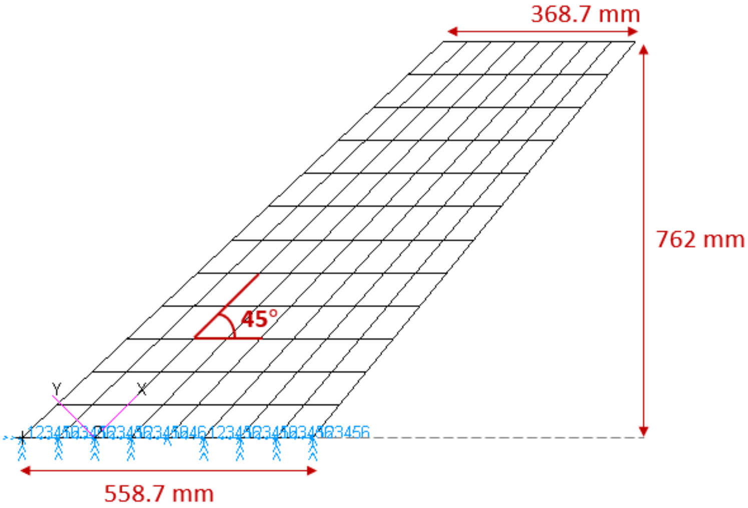

Figure 4.2: Structural finite element model of the AGARD 445.6 wing

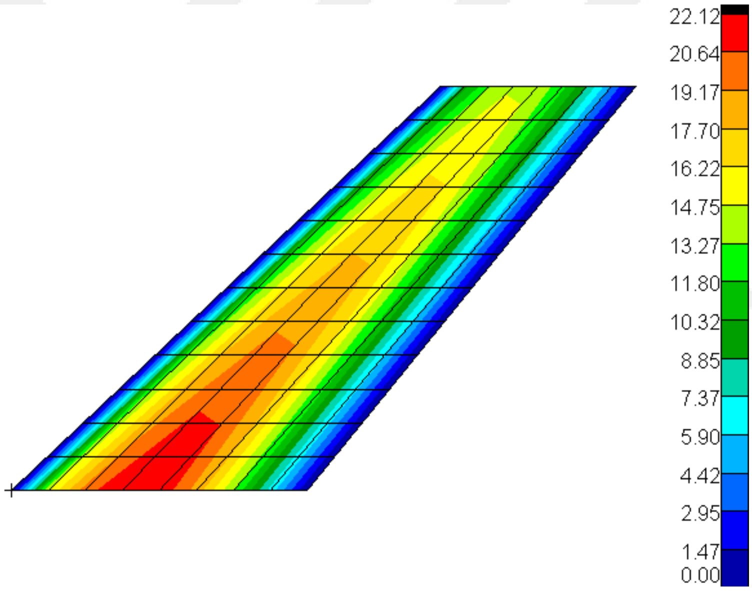

Figure 4.3: Thickness distribution over the AGARD wing model in [mm].

in [18] as well as the computational results of Kolonay [20] since the material properties are taken from that study. It is seen from Table 4.2 that the experimental and modal analysis results are close for the first three modes, where the highest deviation occurs in the 4th mode with a 6.8% difference. On the other hand, the results of the current study are in a good agreement with Kolonay's results for all modes listed in the table. In [19], Yates created the finite element model of the AGARD 445.6 wing in a way that would capture the experimental measurements recorded in previous years

Table 4.1: Material properties used in the weakened AGARD 445.6 wing model [20]

Longitudinal Modulus of Elasticity	E_1	3151.1 MPa
Lateral Modulus of Elasticity	E_2	416.2 MPa
Shear Modulus	G	439.2 MPa
Poisson's Ratio	ν	0.31
Density	ρ	381.98 kg/m^3

and plotted the mode shapes obtained from this model. The mode shapes found as a result of the modal analysis performed in this study are compared with those given in [19] and are found to be compatible. The first and second modes correspond to the first bending and torsion modes of the wing, where the third and fourth are the second bending and torsion modes, as shown in Figure 4.4.

Table 4.2: Comparison of the modal frequencies of the weakened AGARD 445.6 wing model [20]

	Current Study	Experimental (Yates)[18]	Kolonay[20]
Mode 1 [Hz]	9.39	9.60	9.63
Mode 2 [Hz]	38.93	38.10	37.12
Mode 3 [Hz]	48.23	50.70	50.50
Mode 4 [Hz]	91.83	98.50	89.94

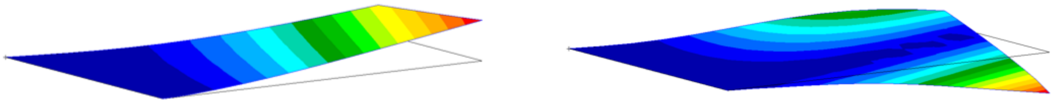

Mode 1, 9.39 Hz

Mode 2, 38.93 Hz

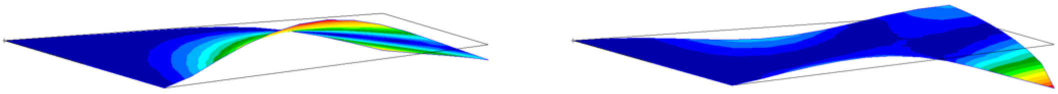

Mode 3, 48.23 Hz

Mode 4, 91.83 Hz

Figure 4.4: The first four mode shapes of the weakened AGARD 445.6 wing

Having shown that the structural model is in an acceptable coherence, the aerodynamic model is created and then coupled with the structural model so that the aeroelastic model of the AGARD wing is obtained to carry out the aeroelastic analysis. The aerodynamic surface is in the same dimensions as the structural model. The panel is divided uniformly into 16 in the chordwise direction and 24 in the spanwise direction, leading to 384 aerodynamic boxes in total. Figure 4.5 demonstrates the aerodynamic mesh.

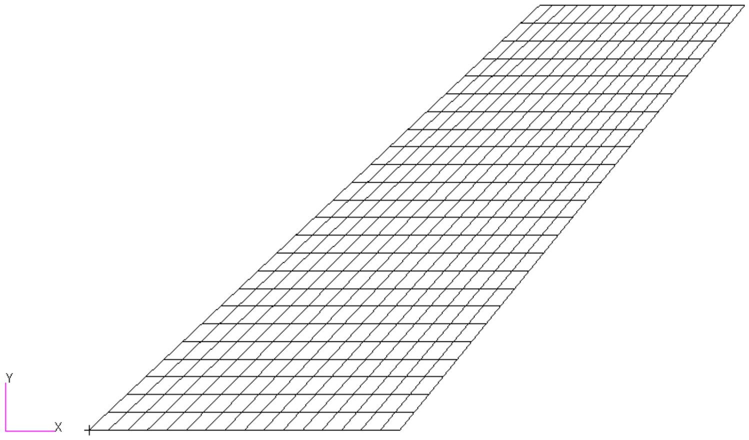

Figure 4.5: Aerodynamic model of the AGARD wing

Force and displacement transformation between the aerodynamic and structural models is enabled by infinite plate splines of Nastran. All the structural nodes are selected for coupling. Spline verification is performed to check if the aerodynamic mesh deforms with the structure. In Figure 4.6 motion of the aerodynamic mesh is shown for the first and second natural modes. It is seen that the aerodynamic model follows the mode shapes of the structure. Therefore, it is concluded that structural and aerodynamic models are coupled properly.

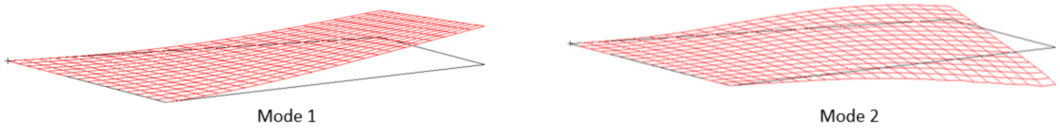
Mode 1

Mode 2

Figure 4.6: Deformation of the aerodynamic mesh for the 1st and 2nd natural modes

4.2 Static Aeroelastic Analysis of the AGARD Wing

In [21], Cai and Liu conducted static aeroelastic analyses of the weakened AGARD 445.6 wing with a coupled computational fluid dynamics (CFD) and computational structural dynamics (CSD) method. Their aerodynamic solution is based on Euler and Navier-Stokes equations. In this case, static aeroelastic analysis of the AGARD wing model described in the previous section is performed by the solver 144 of MSC.Nastran at $M_\infty = 0.85$ and wing angle of attack of 5°as in [21]. Results of the analysis are compared with the ones given in [21] regarding the chordwise pressure distributions for the elastic wing at 34% and 67% spanwise locations and vertical deflections of the leading and trailing edges along the wing span.

In the pressure coefficient (C_p) distribution outcomes of [21], data is available for both the suction and compression sides, as seen in Figure 4.7. However, the aerodynamic method employed in the aeroelastic analysis of this study is a panel method. Therefore, there are no upper and lower surfaces. C_p distribution plots given in [21] are digitized and the pressure difference between the upper and lower sides is calculated so that it can be comparable with the C_p output of MSC.Nastran.

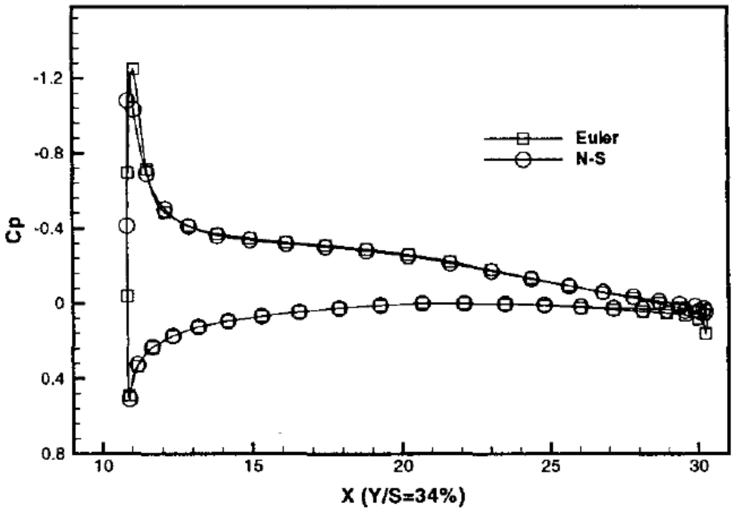

Figure 4.7: C_p distribution at the 34% span for the elastic wing, from [21]

Figure 4.8 shows the pressure difference (ΔC_p) found in this study together with the ΔC_p obtained from [21] at 34% and 67% span locations. Results at 67% span show better agreement; however, for both cases, pressure difference outcomes of this study are compatible with that of [21] except the leading edge. The reason for the mismatch at the leading edge can be different flow solvers or different aerodynamic meshes used in the comparison cases.

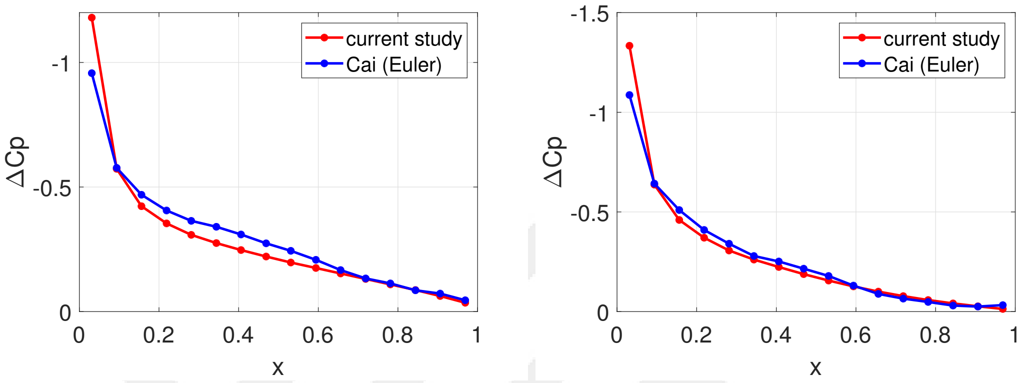

(a) at 34% span

(b) at 67% span

Figure 4.8: Pressure difference comparison for the elastic wing

Comparison of leading edge and trailing edge displacements along the wing span is given in Figure 4.9. Vertical deflection results along the trailing edge fit very well, but the current study leads to higher deflection than [21] at the leading edge. Both approaches confirm that the trailing edge has a greater upward deflection than the leading edge, which leads to a downward twist. The current study predicts a smaller twist angle since the difference between leading and trailing edge deflections is smaller, as seen in Figure 4.9.

In this section, the weakened AGARD 445.6 wing is analyzed by the static aeroelastic solver of MSC.Nastran and the results are compared with the Euler/Navier Stokes based CFD-CSD coupled solution presented in [21]. It is indicated that the general behavior of the results agrees well. The observed deviations are interpreted as reasonable considering the order of aerodynamic solutions employed in different approaches.

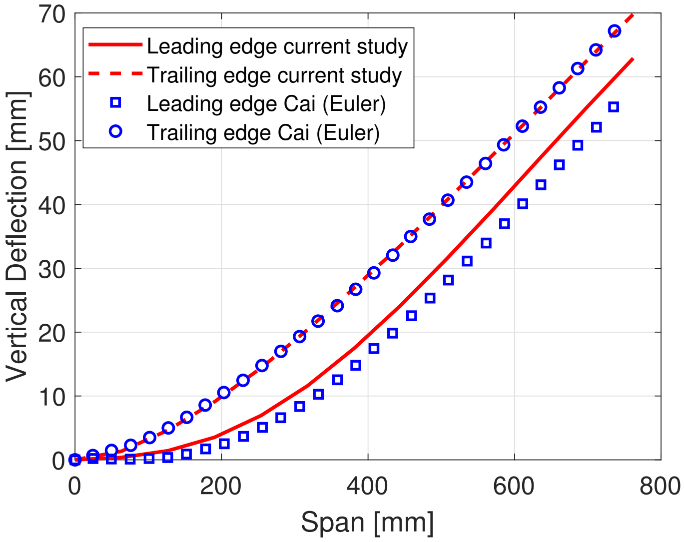

Figure 4.9: Vertical deflection of the leading and trailing edges alond the wing span

4.3 Flutter Analysis of the AGARD wing

Experimental flutter data of the AGARD wing is given in [18]. Wind tunnel tests at various conditions for several wing configurations are available. In this case, data measured in the air for the weakened model 3 at Mach 0.499 and 0.901 are considered. Flutter analysis of the wing model verified in section 4.1 is conducted by solver 145 of MSC.Nastran with the PK method. Structural damping is neglected. The first four modes are included in the flutter solution. Considering that the frequency of the first and the fourth modes are 9.39 Hz and 91.83 Hz, respectively, the frequency range is determined as f_{min}=7 Hz and f_{max}=100 Hz. In the flutter analysis, Mach number, density ratio, velocity range and Mach-reduced frequency pairs need to be specified. The Mach number and air density parameters are taken from the corresponding experimental conditions listed in [18]. Different velocity ranges are selected for the analyses performed at different Mach numbers. The maximum and minimum reduced frequencies are calculated from the following relations and the range between k_{max} and k_{min} is divided into nine equal intervals:

$$k_{min} = \frac{2\pi\, f_{min}\, c}{2\, V_{max}} \quad \text{and} \quad k_{max} = \frac{2\pi\, f_{max}\, c}{2\, V_{min}} \tag{4.1}$$

where reference chord $c = 463.7\, mm$. Details of the analyzed cases are given in Table 4.3.

Table 4.3: Parameters for the flutter analysis.

M	$\rho\,[kg/m^3]$	density ratio	$V_{min}\,[m/s]$	$V_{max}\,[m/s]$	k_{min}	k_{max}
0.499	0.428	0.349	100	200	0.051	1.457
0.901	0.099	0.081	250	350	0.029	0.583

Results of the flutter analysis are examined by looking at the change in damping and frequency with velocity. Figure 4.10 and Figure 4.11 show the damping (g) versus velocity (V) and frequency (f) versus velocity (V) curves of the first four modes at Mach 0.499 and 0.901, respectively. In V-g plots, the point at which damping crosses zero while passing from negative to the positive side is marked as flutter speed. The frequency of the unstable mode at the critical speed is noted as the flutter frequency. For Mach 0.499 case, the flutter speed and the corresponding frequency are found as 176.6 m/s and 23.9 Hz. From the analysis conducted at Mach 0.901 condition, flutter speed and frequency are determined to be 303.7 m/s and 16.7 Hz. In both cases, the first mode is the unstable mode.

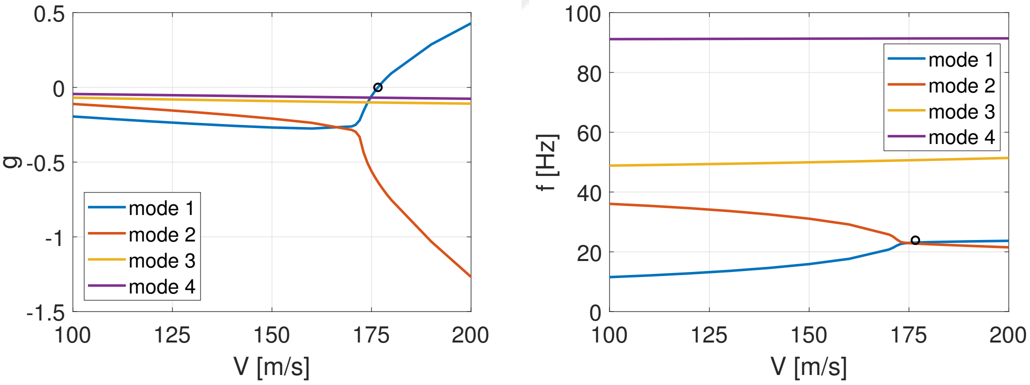

(a) Velocity vs Damping

(b) Velocity vs Frequency

Figure 4.10: Flutter graphs of the AGARD wing for $M = 0.499$

The comparison made in Table 4.4 indicates that the numerical solution ends up with close results to the wind tunnel test data. It is seen that flutter speed estimations are less erroneous than frequency. To sum up, this case study confirms that MSC.Nastran is a reliable option for flutter prediction of the VLA to be analyzed in this thesis.

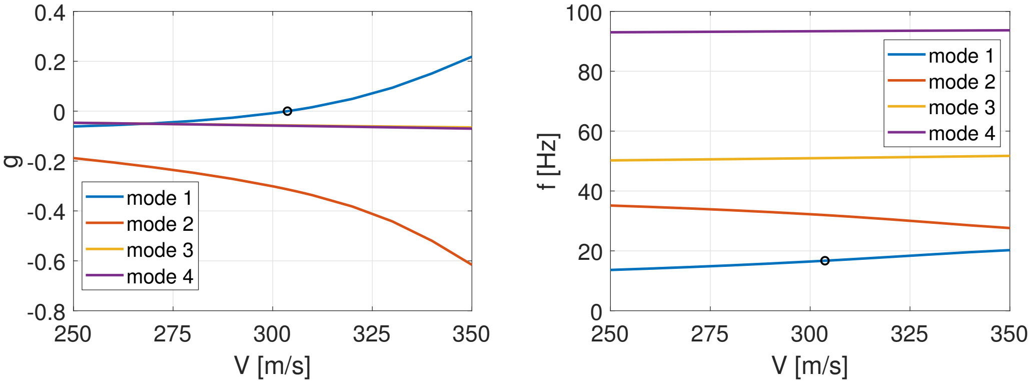

(a) Velocity vs Damping

(b) Velocity vs Frequency

Figure 4.11: Flutter graphs of the AGARD wing for $M = 0.901$

Table 4.4: Comparison of the flutter results with the experimental data

	Flutter Speed [m/s]		Flutter Frequency [Hz]	
Mach	Current Study	Experimental [18]	Current Study	Experimental [18]
0.499	176.6	172.5	23.09	23.39
0.901	303.7	296.7	16.70	16.09

4.4 Discrete Gust Response of the AGARD Wing

In [22], Förster and Breitsamter present two different approaches to predict loads due to discrete gust impact and use AGARD 445.6 wing as a test case. The first approach is referred to as a linear small disturbance frequency domain formulation in which a linear gust model is implemented to the small disturbance CFD-solver, AER-SDNS. The second one is a nonlinear method which is based on the strong coupling of the in-house structural solver, AER-FE, and the in-house transient, nonlinear flow solver, AER-NS. They analyze the weakened model 3 of the AGARD 445.6 wing for "1-cosine" gust excitation at the Mach numbers 0.499, 0.960 and 1.141. The responses of the generalized coordinates corresponding to the first and the second modes are plotted. It is shown that small deviations between the two methods are observed due to transonic effects and the two approaches agree very well in general. In this study, only the Mach 0.499 case is considered. The linear and nonlinear methods implemented in [22] give really close results for the Mach 0.499 case. Results presented in [22] are utilized to validate the discrete gust response analysis performed by solver 146 of MSC.Nastran.

Vertical, "1-cosine" excitation is given as [2]:

$$U = \frac{V_g}{2}(1 - cos\frac{2\pi x_g}{L_g}) \quad \text{where} \quad 0 \leq x_g \leq L_g \tag{4.2}$$

The parameters of the gust analysis are summarized in Table 4.5. The five lowest modes are included in the analysis. The frequency range is specified as 0-120 Hz. The period of the solution is set to be 1 second. Besides, structural damping is neglected in the analysis.

Table 4.5: Parameters of the gust analysis

Mach Number	$M = 0.499$
Air density	$\rho = 0.427648\, kg/m^3$
Free-stream velocity	$U_\infty = 100\, m/s$
Gust velocity	$V_g = 10\, m/s$
Gust Length	$L_{g1} = 5\, m,\ L_{g2} = 50\, m$
Reduced frequency range	$k_{min} \approx 0,\ k_{max} = 2.35$

Discrete gust response of AGARD 445.6 wing is examined in two cases as gust lengths of 5 m and 50 m. Gust length is related to the excitation time and excitation frequency. Gust amplitude is 10 m/s in both cases. As a result of the analysis, modal displacement plots of mode 1 and mode 2 are given side by side with the corresponding results of [22] in Figure 4.12 and Figure 4.13. In Figures 4.12a and 4.13a, SD stands for the linear, small disturbance, frequency domain solution, where NL indicates the nonlinear, time domain solution, respectively.

In [22], it is stated that a maximum wing deflection of 11.5% of the root chord length, i.e., 64.25 mm, is observed in the case of 10 m/s gust amplitude. However, 55.5 mm deflection is detected from the analysis performed by MSC.Nastran. This 13.6% difference is represented in the amplitudes of the responses plotted in Figures 4.12b and 4.12b. Considering that the amplitudes of the modal displacement outputs are arbitrarily scaled, not actual, the outputs of the MSC.Nastran are scaled such that

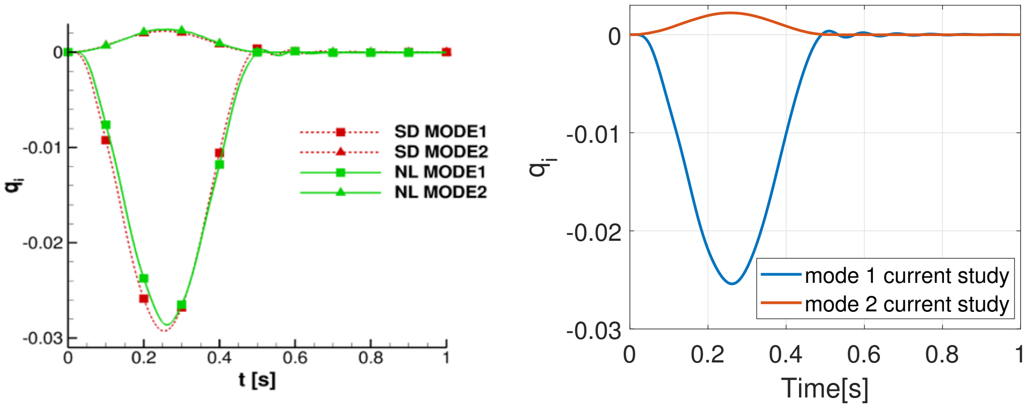

(a) Förster & Breitsamter [22]

(b) Current Study

Figure 4.12: Gust response of the AGARD wing for $L_g = 50m$

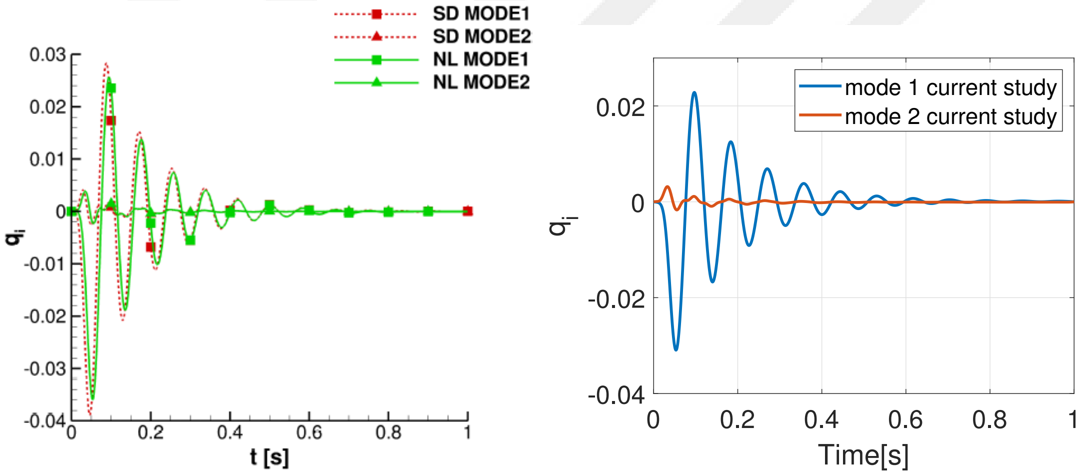

(a) Förster & Breitsamter [22]

(b) Current Study

Figure 4.13: Gust response of the AGARD wing for $L_g = 5m$

they become comparable with the plots of [22]. Nevertheless, the difference between the maximum wing deflection results of two different studies is taken into account while scaling the amplitudes. Thus, this is the reason for the responses obtained from the current study are smaller in magnitude than that of [22], although their general behavior shows a good agreement.

A similar gust response investigation was conducted for the AGARD wing in [35], and the results of the small-disturbance CFD method AER-SDNS are given together with the DLM results. Figure 4.14 is a resultant plot given in [35] showing the gust response of the weakened AGARD 445.6 to a vertical "one-cosine" gust at Mach 0.499. The first mode is shown in blue, where the solid line refers to AER-SDNS results and the dashed line corresponds to DLM results. In addition to aeroelastic response analysis, Vidy et al. [35] compute some rigid aerodynamic derivatives of AGARD 445.6 wing both with AER-SDNS and DLM in order to provide a better understanding of the differences between gust results. They reveal that DLM tends to predict 10% to 15% lower results. Therefore, considering that the aeroelastic response analysis of the current study is based on the Doublet-Lattice Method, differences between the displacement results of the current study and [22] are thought to be expected.

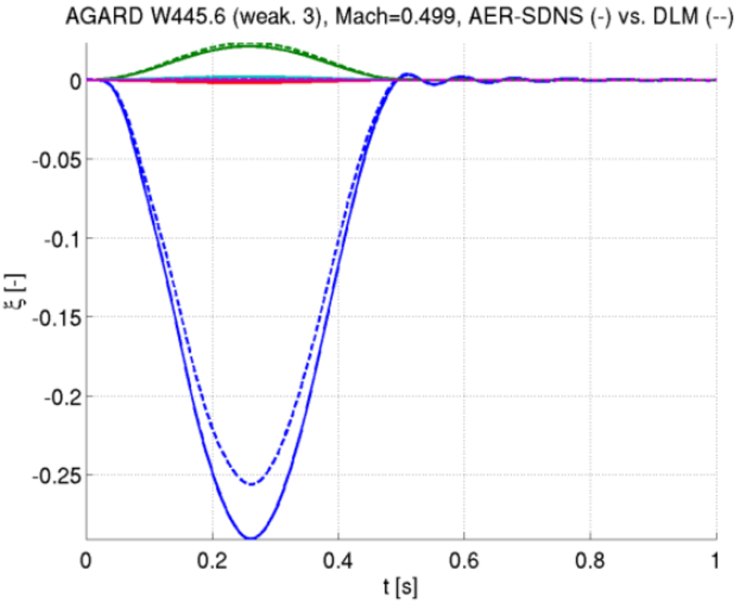

Figure 4.14: Gust response of the AGARD wing, from [35]

CHAPTER 5

AEROELASTIC ANALYSIS OF THE VLA

In this chapter, static aeroelastic, flutter and gust response analyses performed by using the VLA model are explained in detail, and the results are discussed. Firstly, by considering the cantilevered VLA wing only, the effect of DLM correction is shown by comparing the chordwise pressure difference distribution at 34% and 67% spanwise locations that are obtained by CFD and DLM. Secondly, mesh refinement study is carried out for the structural and aerodynamic models, and the models to be used in the aeroelastic analyses of the aircraft are determined. Then, static aeroelasticity results of the VLA are given. In this section, the effect of covering the gap between wing aerodynamic panels, and coupling this panel with the structure on the trim results are shown. The rigid and elastic aerodynamic pressure components over the aerodynamic mesh are demonstrated. The effects of the DLM correction are also examined for the trim solution of the aircraft. Furthermore, aerodynamic loads obtained by CFD analyses are interpolated to the structural mesh. Wing tip displacement and von Mises stress distribution over the wing due to CFD-based loads are compared with the same responses of the structure under DLM-based loads. In section 5.4, details of the flutter analysis are given. Matched-point flutter study is performed. Flutter speed and flutter frequency are listed for various aileron stiffness values. Flutter mode shapes are illustrated. In addition, the change in flutter Mach number with altitude is indicated. Finally, section 5.5 involves the details of the 1-cosine waveform gust profile encountered at the cruise and dive speed conditions in upward and downward directions. The transient vertical acceleration response at the CG of the aircraft and the internal structural loads response at the wing root are examined. Moreover, the change in the responses of the structure with various gust gradient lengths is observed by tuned gust analysis.

5.1 CFD vs. DLM Comparison over the VLA Wing

Wing CFD analyses performed by the project members in the aerodynamics group within the scope of the VLA project are used here to compare CFD and DLM outputs and to see the effect of DLM corrections. Pressure coefficient data obtained from CFD analyses conducted at sea level, Mach 0.156 for 0 and 9 degrees of angle of attack is provided. The cantilevered VLA wing is analyzed at the same conditions with the static aeroelasticity solver of MSC.Nastran, SOL144. In these analyses, the spline is used only to transfer the aerodynamic forces to the structural mesh. Deformation of the structure is not transferred to the aerodynamic mesh since the CFD results also do not include any elastic effects.

0° and 9° angle of attack values mentioned here indicate the aircraft's angle. Therefore, the wing meets the flow with 2 degrees greater angle due to the incidence between the wings and the fuselage. Pressure coefficient distribution through the chord at a certain spanwise location is considered. The pressure difference between the upper and lower surfaces is calculated to be able to make a comparison with the Nastran's pressure coefficient output. CFD and DLM results are compared at two different spanwise locations, 34% and 67%, for various panel mesh densities. Influences of the incidence and camber corrections are shown and it is discussed whether the DLM corrections help the initial DLM solution to be closer to the CFD solution.

First, the zero angle of attack case is studied. Figure 5.1 shows the pressure coefficient variation at 34% wing span. The spanwise location is measured from the root. The horizontal axis represents the x-location normalized with the local chord length. Equally spaced points are specified along the chord and the difference between the upper and lower surface pressure coefficient values at the same point is calculated. Thus, CFD-based ΔC_p distribution shown in Figure 5.2 with red square markers is obtained.

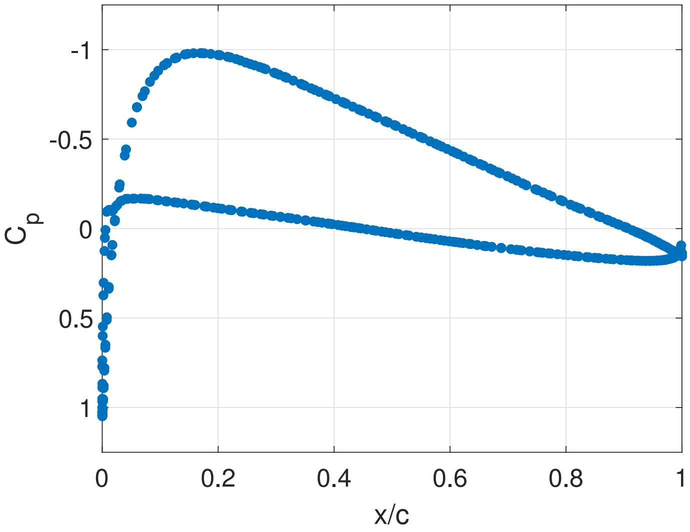

Figure 5.1: C_p distribution obtianed by CFD at 34% span for Mach 0.156 and 0° AoA

Nastran computes zero pressure over the wing aerodynamic elements when the aircraft's angle of attack is set as zero on the trim card. However, the wing has a 2 degree of incidence. Furthermore, the aerodynamic boxes in a chordwise strip have different angles relative to the freestream because of the cambered airfoil. In other words, non-zero pressure should be calculated over the wing even if the aircraft's angle of attack is zero. For this reason, incidence and camber correction is applied to DLM. In Figure 5.2, the individual effects of incidence and camber correction are demonstrated with diamond and hollow circle markers, respectively. The condition at which the CFD result is obtained corresponds to the camber effect added on top of 2 degrees of incidence. Therefore, filled circles in dark blue are the counterpart of CFD results for pressure difference comparison.

It is seen in Figure 5.2 that considering only the incidence effect is not adequate to approach the distribution obtained with CFD and camber correction is also necessary to improve DLM results. Still, the corrected DLM does not fit the CFD output. At the region close to the leading edge, corrected DLM estimates a lower pressure difference than CFD. Two different aerodynamic solutions converge around 0.6 chord and DLM calculates a slightly higher pressure difference than CFD towards the trailing edge. However, this similarity might be considered satisfactory when the distinction between the complexity of compared methods is considered.

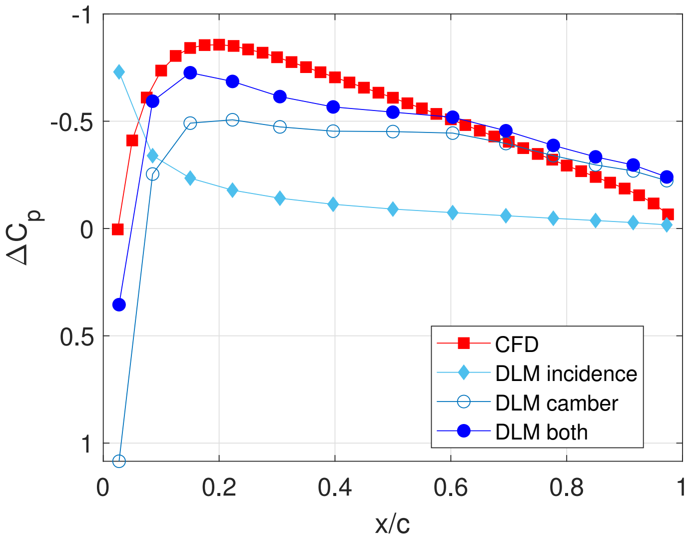

Figure 5.2: Pressure difference comparison at 34% span for Mach 0.156 and 0° AoA

The aerodynamic model, which leads to the results given in Figure 5.2 is taken as baseline mesh. Finer and coarser aerodynamic models are generated by MSC.FlightLoads and the corrected DLM solution is repeated with various panel mesh densities shown in Figure 5.3. The baseline mesh involves 559 aerodynamic elements, whereas coarse and fine meshes include 161 and 1575 elements, respectively. Figure 5.4 demonstrates the effect of mesh refinement on ΔC_p distribution examined at 34% and 67% spanwise locations. It is observed that three different aerodynamic meshes end up with similar results. However, as the number of elements increases, the pressure difference becomes slightly closer to the CFD-based distribution, except the foremost data point. Moreover, CFD versus corrected DLM comparisons made at 34% and 67% span looks very similar overall, as shown in Figures 5.4a and 5.4b. It can be said that the conformity at the points close to the leading edge is better at 67% wing span and the results of the two methods intersect at an earlier chordwise position at 67% span. As a result, the DLM's capability of capturing CFD results does not differ considerably with the spanwise location, in this case.

Secondly, the case with 9° of angle of attack is investigated. Figure 5.5 illustrates the pressure coefficient outcome of CFD at 34% wing span for 9° of aircraft's angle of attack or, in other words, 11° of wing angle of attack. Similarly, the pressure difference between the upper and lower wing surfaces are shown in Figures 5.6a and 5.6b

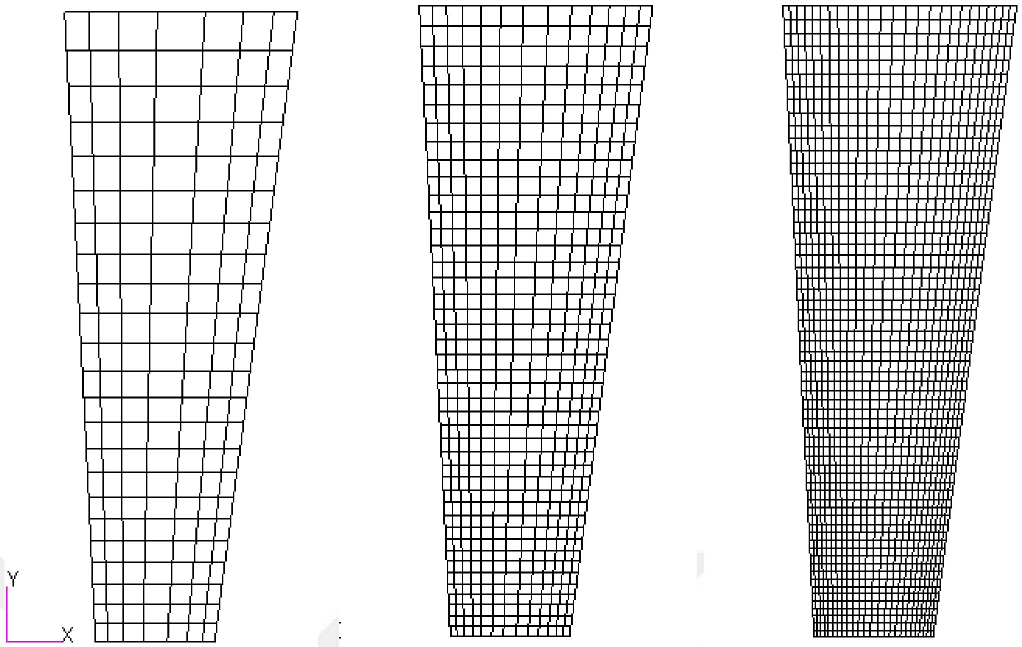

(a) coarse mesh (b) baseline mesh (c) fine mesh

Figure 5.3: Aerodynamic models of DLM analyses with different mesh densities

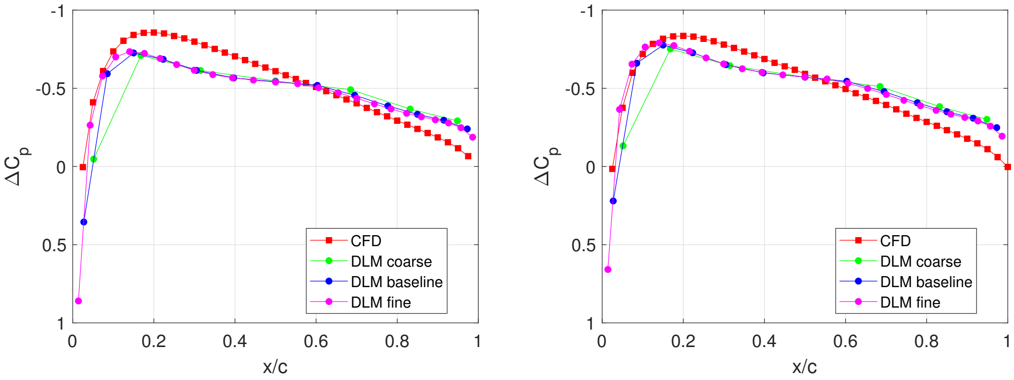

(a) at 34% wing span (b) at 67% wing span

Figure 5.4: Pressure difference comparison at 34% and 67% spanwise locations with various panel mesh density for Mach 0.156 and 0° AoA

with red square markers. This time, only the fine aerodynamic mesh is analyzed with MSC.Nastran and the results are given only at 34% wing span since it is previously concluded that the fine mesh gives slightly better results and CFD-DLM comparison is not highly sensitive to the choice of spanwise location.

Figure 5.6 presents two alternative ways that reach the same endpoint. In Figure 5.6a, the analysis is first conducted by dictating 9° angle of attack input and represented with yellow diamond markers. Then, both camber and 2° of incidence correction are applied to this solution and given in dark blue circles. On the other hand, in Figure 5.6b, the analysis is performed at an 11° angle of attack and only the camber correction is applied to this solution, shown in orange diamonds and dark blue circles, respectively. Results given in dark blue circles in both Figures 5.6a and 5.6b are identical, which means that dictating an additional 2° angle of attack as an analysis condition or adding an incidence of the same amount to each aerodynamic box results in the same way.

When it comes to the comparison of the corrected DLM with CFD, again, DLM underestimates the pressure difference around the leading edge. At around 0.6 chord, results intersect and DLM yields slightly greater pressure difference through the trailing edge. It can be said that the camber effect makes the DLM-based distribution relatively closer to the CFD-based distribution.

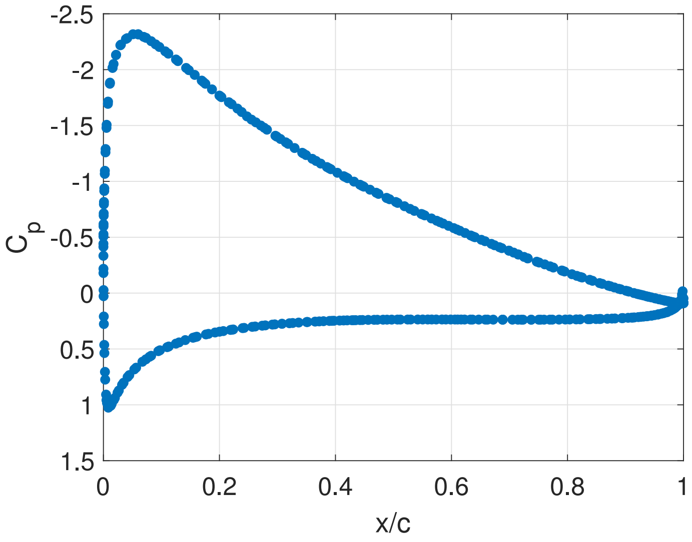

Figure 5.5: C_p distribution at 34% span for Mach 0.156 and 9° AoA

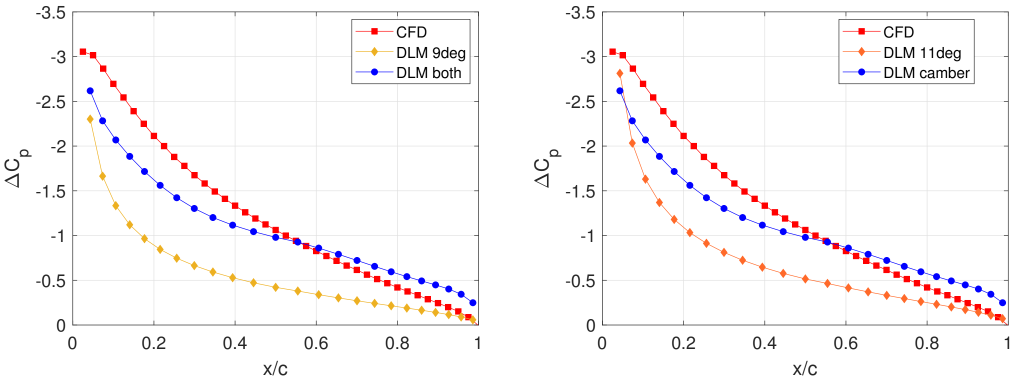

(a) analysis performed at 9° AoA (b) analysis performed at 11° AoA

Figure 5.6: Pressure difference comparison at 34% span with fine mesh for Mach 0.156 and 9° AoA

5.2 Mesh Refinement Study

In this section, mesh convergence study is conducted for both the structural and aerodynamic models. First, the mesh density of the structural model is determined by observing the change in modal frequencies with the increasing number of structural elements. Having decided the structural mesh, aerodynamic mesh refinement is performed. Static aeroelasticity, flutter and discrete gust response outputs are tabulated for three different aerodynamic mesh densities where the structural model used in the aeroelasticity remains constant. The structural and aerodynamic meshes decided here are used in the subsequent aeroelastic analyses mentioned in sections 5.3, 5.4 and 5.5.

5.2.1 Structural Model

The global finite element model (GFEM) is considered as the baseline and it is intended to determine the structural mesh density by checking the convergence of the modal frequencies as the number of elements increases. For this purpose, the structural aircraft model is refined by increasing the number of 2D elements by four and 1D elements by two. However, local modes are encountered as a result of the modal analysis of the refined model, as shown in Figure 5.7. When a quadrilateral element is considered, breaking the element into 4, by dividing it crosswise and longitudinally, leads to a new node appearing at the center of the element. This node is not supported by any structural members such as ribs, stiffeners, etc. As a result, local modes occur due to increased degrees of freedom induced by newly generated nodes. Local modes prevent tracking certain modes of the GFEM and observing how the modal frequencies of the same modes change as the mesh density increases. Furthermore, the occurrence of the local modes disturbs the dynamic aeroelasticity outputs. Hence, it is concluded that using a structural model refined in this manner in the aeroelastic analyses is not applicable.

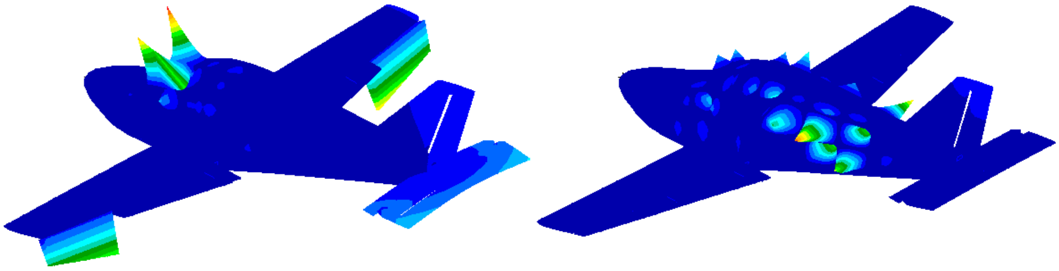

(a) Local mode & aileron coupling (19.3 Hz)

(b) Local mode at the fuselage (32.7 Hz)

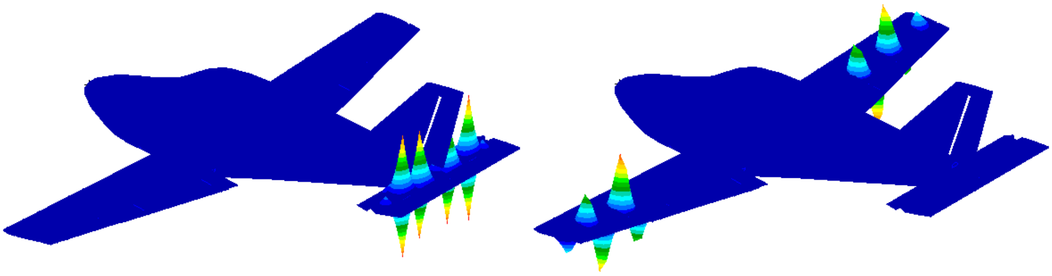

(c) Local mode at the horizontal tail (47.1 Hz)

(d) Local mode at the wings (50.1 Hz)

Figure 5.7: Local modes of the refined model

[36] mentions a similar problem within the mesh study of the fighter wing analyzed in that study. An alternative mesh refinement approach eliminating local modes is implemented in [36]. 2D shell elements are divided in only one direction such that nodes of the new elements are supported by spars or ribs. In this case, the cantilevered VLA wing is considered rather than the whole aircraft model. Shell elements are broken into two from the edges in the chordwise direction such that newly created nodes coincide with the ribs. Figure 5.8 shows the coarse GFEM mesh and the refined mesh. This approach enables to compare the modal frequencies of the wing for the coarse and fine meshes; yet, it has some drawbacks. Aspect ratios of the shell elements increase since the elements are divided only in one direction. A further refined, third model is not analyzed since the elements of that model would be more slender, which is an undesirable situation. Moreover, the number of 2D elements in skins and ribs is increased only, whereas the 2D elements in spar webs and 1D elements throughout the wing remain the same. After all, the total number of CQUAD4 and CTRIA3 elements is increased from 473 to 797 leading to an increase in the total number of structural elements from 898 to 1222. The frequencies of the first four normal modes of the cantilevered wing are compared in Table 5.2 for two different mesh densities. It is seen that the modal frequencies are not highly sensitive to mesh density. The highest difference between the frequencies of the coarse and fine wing models is seen for the fourth mode by 2.43%, where the differences for the first three modes are below 2%. Based on this study conducted for the wing, it is decided to continue the aeroelastic analyzes using the GFEM mesh for the whole aircraft model.

Table 5.1: Comparison of the modal frequencies of the cantilevered VLA wing for two different mesh density

		Coarse Model	Refined Model	% Difference
Mode 1	1st bending	13.42 Hz	13.26 Hz	1.67 %
Mode 2	In-plane bending	49.51 Hz	49.58 Hz	0.14 %
Mode 3	2nd bending	54.77 Hz	53.99 Hz	1.44%
Mode 4	Torsion	110.83 Hz	108.20 Hz	2.43%

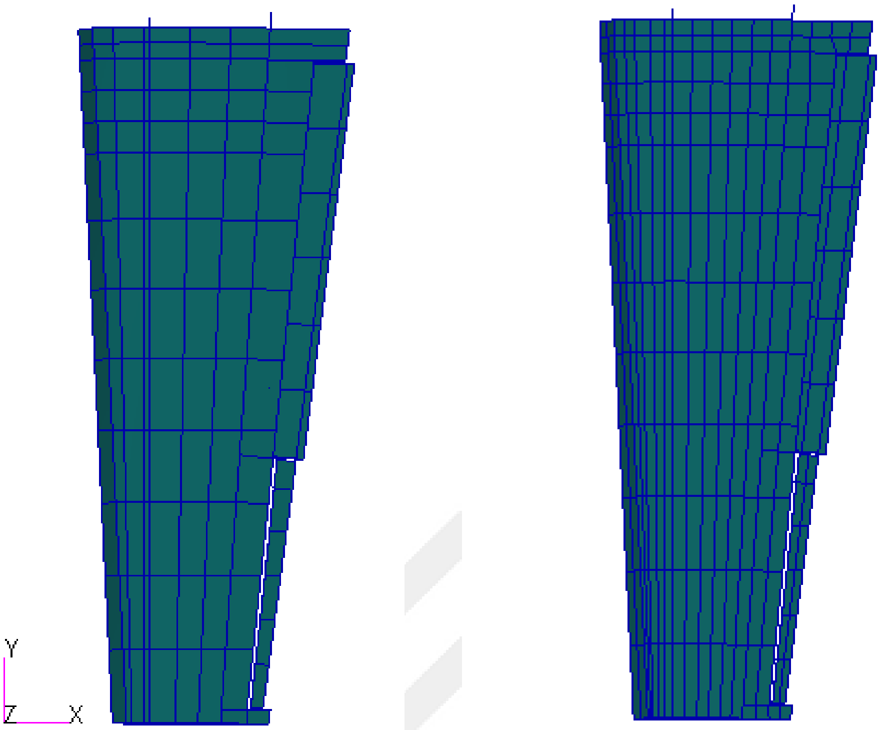

(a) coarse wing mesh

(b) refined wing mesh

Figure 5.8: Wing structural models with GFEM element size and reduced element size

5.2.2 Aerodynamic Model

The aerodynamic model described in section 2.2 is taken as the baseline and coarser and finer versions are modeled. Coarse, baseline and fine aerodynamic models are analyzed in all aeroelastic analysis types examined in this thesis. By looking at the variation of analysis results with the aerodynamic mesh density, it is aimed to determine the aerodynamic model to be used in the aeroelastic analyses given in detail in the following sections.

Coarse, baseline and fine aerodynamic meshes are displayed in Figure 5.9. The coarse model involves 454 aerodynamic boxes, where baseline and fine aerodynamic models contain 1604 and 5476 boxes, respectively. Static aeroelastic analysis, flutter and discrete gust response analysis are performed by coupling all three aerodynamic models with the same structural model, which is the GFEM as decided in the previous section. In the following sections, variations of the aeroelastic model are discussed, such as covering the gap between the wings with aerodynamic panels, whether to spline this bridging panel with the structure or not, applying the DLM correction, etc. However, here a basic configuration is used for mesh density comparison in which no DLM correction is applied yet and wing bridging aerodynamic panel is coupled with the structure.

Table 5.2 presents the comparison of static and dynamic aeroelastic analysis results obtained with coarse, baseline and fine aerodynamic models. In static aeroelasticity, 3.8g pull-up maneuver at dive speed is analyzed at 7500 feet altitude and trim angles, wingtip displacement and the maximum von Mises stress over the wing are listed. Flutter speed and flutter frequency are the outputs of the flutter analysis performed at the sea level, Mach 0.0 condition. In addition, 1-cosine gust at 7500 feet is considered at the cruise speed and the highest positive and negative vertical acceleration at the CG of the vehicle are included in the comparison. Explanations about these analyses and detailed results are given in sections 5.3, 5.4 and 5.5.

Table 5.2: Effect of mesh density on aeroelastic analyses results

		Coarse	**Baseline**	**Fine**
Static Aeroelasticity	Trim angles	AoA= 8.22° elev.=2.50°	AoA= 8.26° elev.=2.17°	AoA= 8.29° elev.=1.96°
	Wingtip disp.	78.1 mm	77.3 mm	76.8 mm
	Max. wing stress	120 MPa	119 MPa	118 MPa
Flutter	Flutter speed	201 m/s	201 m/s	203 m/s
	Flutter frequency	47.64 Hz	47.58 Hz	47.54 Hz
Discrete Gust Response	Max. vertical acceleration	+4.16g -2.16g	+4.15g -2.15g	+4.15g -2.15g

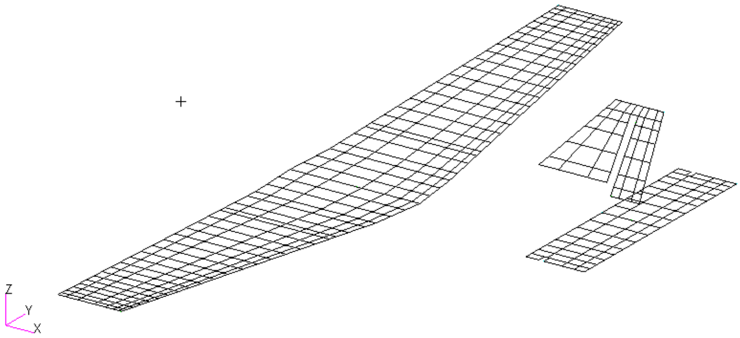

(a) Coarse aerodynamic mesh

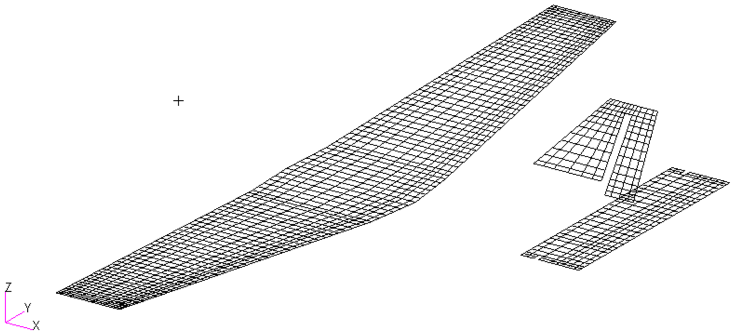

(b) Baseline aerodynamic mesh

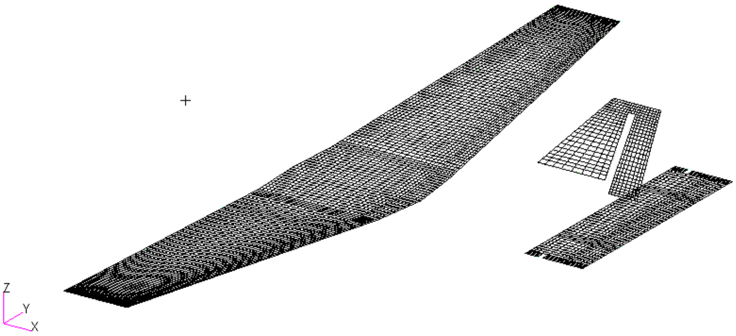

(c) Fine aerodynamic mesh

Figure 5.9: Aerodynamic models analyzed to determine mesh density

It is seen from Table 5.2 that flutter and gust response results show really minor changes for three different mesh densities. On the other hand, more notable differences are observed in static aeroelasticity results compared to the dynamic analysis results. Although the trim angle of attack does not change considerably, elevator angle, wingtip displacement and the maximum stress at the wing reduces slightly as the number of aerodynamic elements increases. In mesh refinement studies, computation time is also considered. Baseline mesh does not cause any suffering from run times. However, switching to the fine model results in a great difference in the execution time of especially the dynamic aeroelastic analyses, since all the lifting surfaces are refined and the number of aerodynamic boxes increased remarkably. For instance, the execution time for the flutter analysis increased from 1 to 25 minutes when the fine model is used instead of the baseline model. A 25-minute analysis may not sound too long, but a further highly refined model can not even be solved with current computer hardware due to lack of memory. As a result, considering the computational cost of the fine mesh and the similarities presented in Table 5.2, the baseline aerodynamic model is evaluated as a reasonable option.

Thus, it is determined to use the global finite element model and the baseline aerodynamic model as the structural and aerodynamic models of the aeroelastic analysis. Detailed discussions on the analyses performed with these models take place in the following sections.

5.3 Static Aeroelasticity Results

Solution sequence of MSC.Nastran for static aeroelasticity, SOL 144, is used and the flexible trim method is selected for the static aeroelastic analysis presented in this study. It calculates the trim parameters and the resulting external loads on the aircraft.

Pull-up maneuver at a limit maneuver load factor, 3.8g, at 7500 feet and dive speed is analyzed. Mass and CG of the original structural finite element model of 715 kg are adjusted for this case because outputs of the CFD analyses performed for 750 kg aircraft are referred for comparison purposes. The mass of the initial GFEM is increased by adjusting the masses of the concentrated mass elements in a way that the CG location of the adjusted model matches the CG input of the CFD analysis. Thus, a model to give more suitable results for the comparison of different methods is obtained. The mass adjustment is applied only to the static aeroelastic analyses mentioned in this section. For flutter and gust response analyses, the structural model is used as-is.

For static aeroelasticity, Nastran requires one or more structural degrees of freedom to be identified for inertia reaction [23]. The node located at the CG is chosen as the structural point, and translation in the vertical direction and pitching about y-axis degrees of freedom are specified for rigid body motion to apply SUPORT boundary condition. Single point constraint is applied to the CG node in degrees of freedom other than vertical translation and pitching. Considering that the flight case is a symmetric maneuver, angle of attack and elevator rotation are set as free trim parameters to be determined as a result of the static trim analysis. Table 5.3 lists the input parameters used.

Table 5.3: Input trim parameters

n_z	3.8 g
Mach number	0.238
Dynamic pressure	3062 Pa
Rigid body motion parameter	Angle of attack
Control surface	Elevator

Three distinct models differing from each other in terms of handling the gap between the wings are analyzed and the results are given in Table 5.4. In the first model, wing aerodynamic panels are not extended and the gap is not covered. In the second model, the gap is covered with the wing bridging panel, but the panel is not splined to the structure. Lastly, in model 3, the wing bridging panel is coupled with the structural nodes located on the front and rear spars passing through the fuselage. When a panel connecting the wings is included in the aerodynamic model but not coupled with the structure, the aerodynamic forces produced by that panel are not transferred to the structure. Therefore, the contribution of this bridging panel is not accounted for in the aerodynamic forces that will balance the inertia in the trim analysis. This explains the difference between the results of the second and the third models. In the case of model 3, the trim condition can be satisfied at lower angles with the contribution of the aerodynamic forces arising from the bridging panel. Even though the bridging panel itself is not included in trim calculations when it is not splined, the presence of the panel changes trim results. This can be seen by comparing the results of models 1 and 2 in Table 5.4. The change in the pressure distribution over the inboard sections of the wings due to the presence of the bridging panel is illustrated in Figure 5.10. In model 2, the bridging aerodynamic panel prevents the unrealistic aerodynamic solution due to the gap at the wing roots. Therefore, model 1 is not an option due to unacceptably high trim angles. In this study, aerodynamic modeling of the fuselage is not performed. In order to account for the aerodynamic contribution of the fuselage, model 3 is preferred to be used in the subsequent analyses.

Table 5.4: Trim results for different wing bridging approaches

	model 1: no bridge	model 2: bridge not splined	model 3: bridge splined
Trim angle of attack	13.6 °	10.3 °	8.3 °
Elevator rotation (upward)	20.6 °	4.1 °	2.2 °

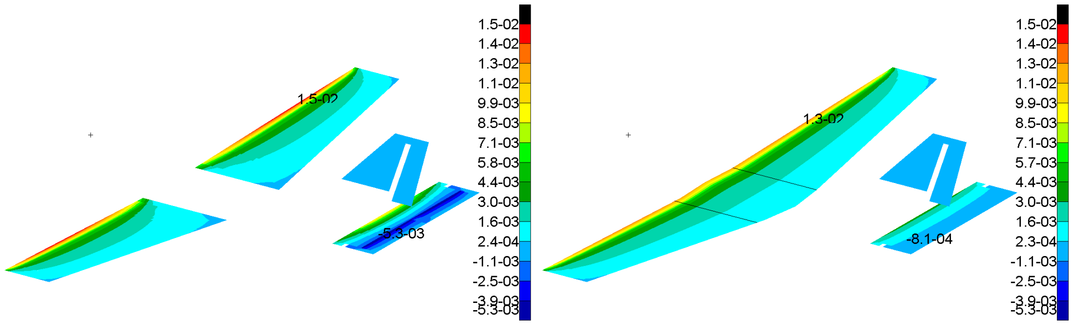

(a) model 1

(b) model 2

Figure 5.10: Pressure distributions [MPa] over the aerodynamic meshes of models 1 and 2

Having decided to proceed with the aeroelastic model 3, first, an analysis is performed without any intervention to the aerodynamic theory and the results of this analysis are given as the ones without DLM correction. Then, slope input accounting for the wing camber and incidence is given for each wing aerodynamic element and results obtained with this approach are presented as the ones with DLM correction.

Deformation of the aerodynamic mesh is one of the outputs to be checked. The aerodynamic mesh is deformed by transferring the displacement of structural nodes with the help of splines. Figure 5.11 depicts the deformation of the aerodynamic model when DLM correction is applied. The maximum displacement of almost 90 mm is seen at the wing tip. Tip deflection reduces to 82 mm for the case in which initial downwash is ignored.

Pressure over the aerodynamic mesh is visualized in Figure 5.12. These plots enable to see the effect of wing incidence and camber on the pressure distribution and also to compare the rigid and elastic parts of the aeroelastic pressure. The aerodynamic pressure distribution calculated without taking the deformation of the model into account is given as the rigid component of aeroelastic pressure, where the elastic component indicates the incremental pressure due to the deformation of the elastic structure. The elastic component of pressure is lower in magnitude since it represents the additional effect coming from the flexibility. For both of the cases with or without DLM correction, it can be seen that the negative elastic pressure values are more significant in

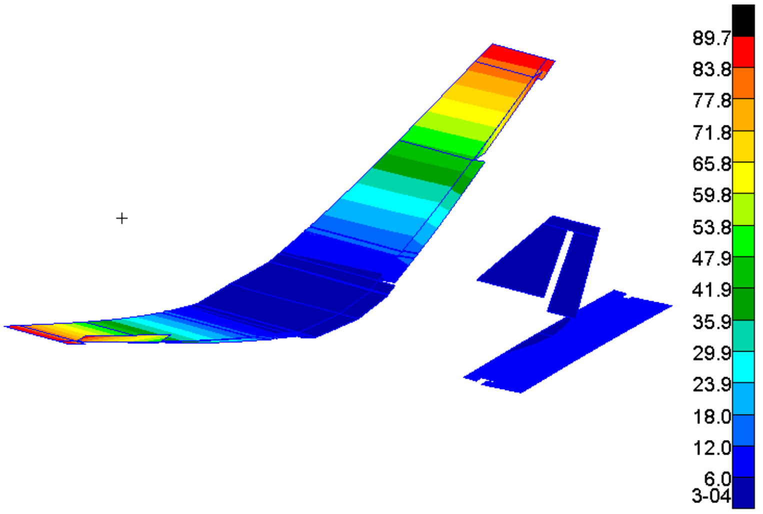

Figure 5.11: Deformed aerodynamic mesh [mm] with DLM correction

magnitude than the positive ones. A different distribution in the aileron region from the rest of the wing draws attention in Figures 5.12c and 5.12d. This is because of the motion of that surface due to the flexibility in the aileron connection. The elastic pressure component becomes more remarkable when DLM correction is applied. Moreover, in Figure 5.12c, the elastic component of the pressure distribution over the wings is relatively uniform, while variation in distribution can be seen in Figure 5.12d when DLM correction is applied. Lastly, by looking at the major component of pressure from Figures 5.12a and 5.12b, it can be observed that the maximum pressure value seen at the wing leading edge decreases with DLM correction. However, moderate pressure regions shown in greens and light blues expand in chordwise direction when wing incidence and camber effect are included. Furthermore, the distribution pattern over the wings is not followed by the bridging panel in 5.12b. This arises from the fact that DLM correction is applied only to the wing panels.

On the side, CFD analysis of the VLA is conducted in Ansys Fluent by members of the project's aerodynamics group to produce aerodynamic forces balancing the 750 kg aircraft undergoing 3.8g acceleration. For this purpose, for different incidence and elevator angles, CFD analyses are performed and trim condition for the 3.8g dive speed condition is determined iteratively. Thus, trim angles are found as 1.5° angle of attack and 0.7° elevator angle from CFD analyses. Loads obtained from CFD are interpolated to the global finite element model and linear static analysis is performed

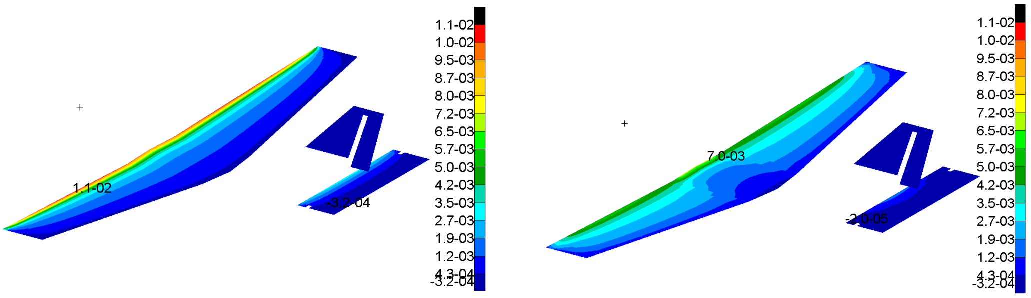

(a) Rigid component without DLM correction (b) Rigid component with DLM correction

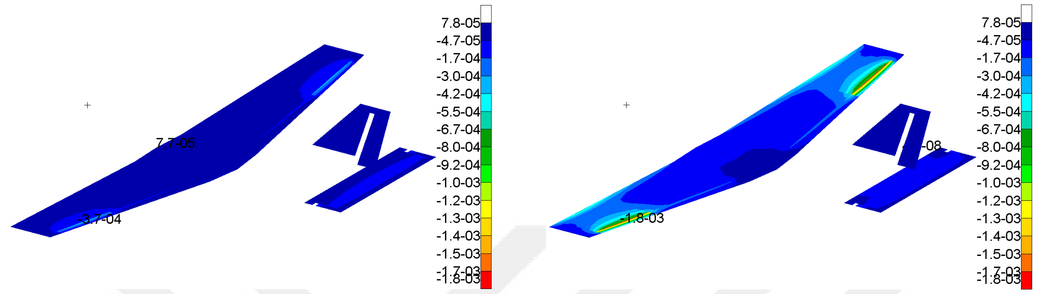

(c) Elastic component without DLM correction (d) Elastic component with DLM correction

Figure 5.12: Rigid and elastic components of aeroelastic pressure in [MPa] with and without DLM correction

in Nastran by incorporating inertia relief. Response of the structure subjected to CFD-based aerodynamic loads is observed by looking at the wing tip displacement and von Mises stress distribution over the main wing structure. Wing tip displacement under CFD-based loads is measured as 80 mm. Figure 5.13a demonstrates that stress concentration occurs at the wing root around the front spar and the maximum von Mises stress value over the wing is 129 MPa.

Table 5.5 lists the static trim results with aeroelastic model corrections implemented step by step. Analysis results are obtained by adding the modifications given in each new column to the previous case. It is seen from Table 5.5 that applying DLM correction to account for camber and incidence of the wing causes a reduction in trim angles but an increase in the response of the wing structure. Lower trim angles are expected since including the camber and incidence results in higher lift generation, and the aerodynamic forces can balance the inertia of the aircraft at lower values of angle of attack and elevator rotation. The total amount of aerodynamic forces generated by the

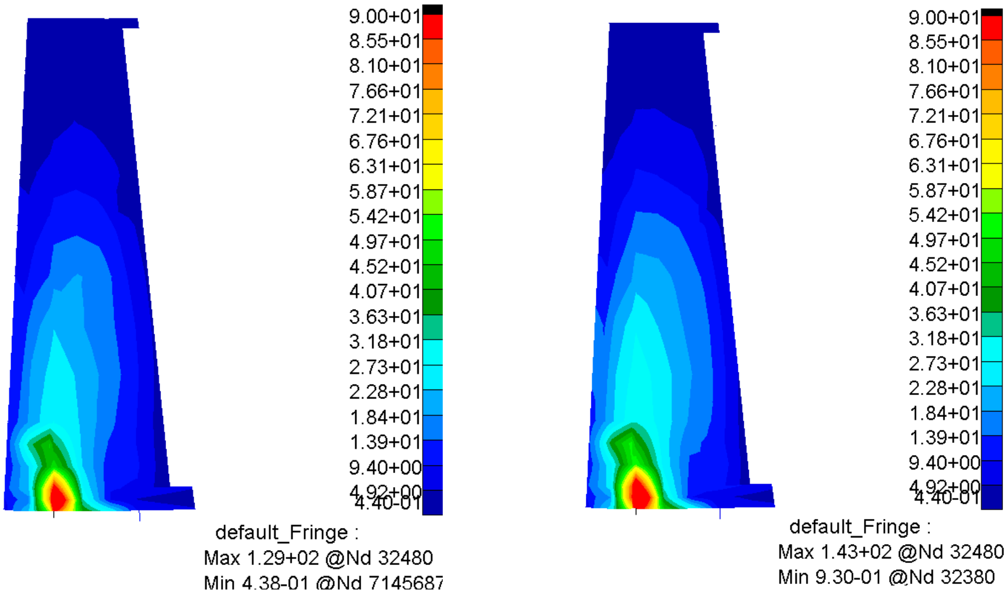

(a) CFD-based

(b) DLM-based

Figure 5.13: Von Mises stress distribution over the wing. DLM based results correspond to the case given in the last column of Table 5.5.

Table 5.5: Static trim outputs for different analysis cases

	Wing Bridge Splined	DLM Correction	Spline Usage: Force only
AoA [deg]	8.3	3.9	3.3
Elevator angle [deg]	2.2	0.1	0.7
Tip disp. [mm]	77	89	112
Max. stress [MPa]	119	132	143

lifting surfaces composing the aerodynamic model remains constant. However, DLM correction makes wing surfaces produce a greater portion of the total force. Greater forces arising from the wing aerodynamic elements are carried by the wing structural model. This explains the higher wing tip displacement and von Mises stress values compared to the previous version.

Finally, spline usage preference is changed from both force and displacement transformation to the force transformation only. In other words, aerodynamic forces are applied to the structure from aerodynamic panels which are intended not to move [26]. Linear static analysis with CFD loads is a one-way analysis in which structural deformations do not affect aerodynamic load calculations. Therefore, it would be appropriate to prefer a rigid aerodynamic solution in static trim analysis to make a better comparison. Considering the 80 mm tip displacement and 129 MPa maximum stress values calculated with CFD loads, Table 5.5 shows that when the force spline method is used, the resulting tip displacement and maximum von Mises stress values obtained by using the DLM-based loads deviate more from the corresponding values obtained by CFD-based loads. However, there is a considerable difference between the two methods in terms of including the fuselage effect in aerodynamic calculations. The current aerodynamic model used in the static trim analysis consists of only lifting surfaces, whereas CFD analysis involves the fuselage as well. CFD analysis indicates that the fuselage generates lift. In static aeroelastic analysis, the missing contribution of the fuselage needs to be compensated for by the lifting surfaces. As a result, the higher structural response under DLM-based loads may be due to the excessive role of the wing in this aero-modeling approach.

To enable a fair comparison, aerodynamic modeling of the fuselage in the static aeroelastic analysis is intended. Beam spline type is required to couple the aerodynamic body elements to the structure; however, the fuselage should be represented by a stick model to use this type of spline. The creation of a stick model that represents the existing 3-dimensional fuselage model is considered to be beyond the scope of this thesis. The contribution of the fuselage aerodynamic body is not included in trim calculations as long as it is not splined to the structure. Therefore, this is the limitation of this study and coupling of the aerodynamic fuselage model and structural stick model can be noted as a future study.

In Figure 5.13b, von Mises stress distribution for the case given in the last column of Table 5.5 is illustrated. The stress concentration locations are the same for CFD-based and DLM-based loads and the stress distributions are found to be similar.

Table 5.6: Static trim outputs without DLM correction

	Wing Bridge Splined	Spline Usage: Force
AoA [deg]	8.3	8.2
Elevator angle [deg]	2.2	2.6
Tip disp. [mm]	77	73
Max. stress [MPa]	119	121

Furthermore, aeroelastic effects on the static trim solution can be interpreted by comparing the results of the last two steps given in Table 5.5. Although the trim angles are not highly affected, displacement and stress values seem to reduce significantly by the aeroelastic interactions. In order to investigate the influence of DLM corrections on the difference between rigid and aeroelastic cases, Table 5.6 gives the outputs when the DLM correction step is removed. It is revealed that eliminating aeroelastic effects by changing the spline usage preference to only force transformation causes fewer differences in the static trim results when the DLM correction is not applied.

5.4 Flutter Results

Flutter is a dynamic aeroelastic stability problem, and it requires complex eigenvalue solutions. Flutter solver of MSC.Nastran, SOL 145, provides a couple of solution methods as PK, K, PKNL, and KE. PK method is employed in this study, which computes flutter roots for density, Mach number and velocity values which are provided as input by the user [26]. The iteration process is conducted over the reduced frequency calculations and convergence of the reduced frequency is checked to finalize the iterations. In the PK method, unsteady aerodynamics is restricted to simple harmonic motion. Flutter solution by the PK method ends up with complex roots in which the imaginary part represents the frequency and the real part corresponds to damping. Roots with a positive real part, $g > 0$, point out an instability in the system.

Flutter solution is sensitive to control surface modeling. In this study, the unknown torsional stiffness values are arbitrarily defined by considering the resultant dynamic behavior of the control surfaces, as explained in Section 2.1. Here, the effect of aileron stiffness on flutter solution is investigated. First, the wing structure is isolated and the change of flutter results with varying torsional stiffness of the aileron is presented. Then, the dynamic stability of the full vehicle model is discussed. Aileron stiffness investigation is performed also for the aircraft flutter analysis. In addition, the change in flutter Mach number with altitude is shown.

5.4.1 Flutter Analysis of the Isolated Wing Model

The flutter analysis of the cantilevered VLA wing is conducted at sea level for zero Mach number. The modes with frequencies up to 120 Hz are included in the calculations. The velocity range is set as from 20 m/s to 300 m/s. The dive speed of the VLA is 70.7 m/s; however, the velocity range is extended to 300 m/s to detect flutter occurrence.

In the flutter analyses, rotation of the flap is prevented to highlight the influence of wing-aileron coupling. In the control surface modeling step, 10 kNm/rad of torsional stiffness was determined for the ailerons, which resulted in the aileron rotation modes with about 15 Hz of frequency. The assumed aileron stiffness will be referred to as

k_t, and taking the case with k_t as a baseline, flutter analysis is carried out with higher and lower aileron stiffness.

For all the cases, first, the input parameters of zero Mach number and sea level air density are provided. The Mach numbers corresponding to the flutter speeds obtained as a result of the initial analyses are calculated. Then the analyses are repeated for the found Mach numbers. Thus, a matched point study is conducted by doing iterative analyses until the input and resultant Mach numbers converge.

In Table 5.7, flutter results at the sea level for the aileron stiffness of 0.5, 1.0, 2.0, 3.0 times k_t are given as well as for the cases in which ailerons are fixed and free. Free aileron and fixed aileron cases are obtained by giving a very low and very high stiffness input. Table 5.7 lists the outputs of the analysis with the 0.0 Mach number and the matched flutter solutions. In Table 5.7, the results of the wing torsion modes are presented. However, for the $0.5k_t$ and free aileron cases, the frequency of the aileron rotation mode approaches that of the wing bending mode and at very low speeds such as 20 m/s or 40 m/s, instability is seen due to the coupling of the wing bending and aileron rotation modes. However, as the velocity increases, damping returns back to the negative side. Moreover, this low-speed instability issue is not encountered for the cases where the aileron torsional stiffness is k_t or higher.

Table 5.7: Sea level flutter analysis outputs of the wing for different torsional stiffness of the aileron

Aileron	**Mach 0.0 Solutions**			**Matched Solutions**		
Stiffness	V_f [m/s]	f_f [Hz]	M_f	V_f [m/s]	f_f [Hz]	M_f
aileron free	137.9	77.1	0.406	153.7	76.9	0.452
$0.5k_t$	139.8	77.0	0.411	155.2	76.9	0.456
k_t	138.0	77.1	0.406	153.3	76.9	0.451
$2.0k_t$	134.5	77.2	0.396	149.5	76.9	0.440
$3.0k_t$	131.3	77.3	0.386	145.8	77.0	0.429
aileron fixed	141.5	76.2	0.416	173.4	76.5	0.510

Figure 5.14 demonstrates the damping and frequency variation of the unstable mode with the velocity for different values of aileron torsional stiffness. Matched flutter speeds listed in Table 5.7 indicate the points at which V-g curves cross zero while damping passes from negative to positive in Figure 5.14a. Furthermore, in Figure 5.14b, flutter frequencies correspond to the values seen at the critical speeds.

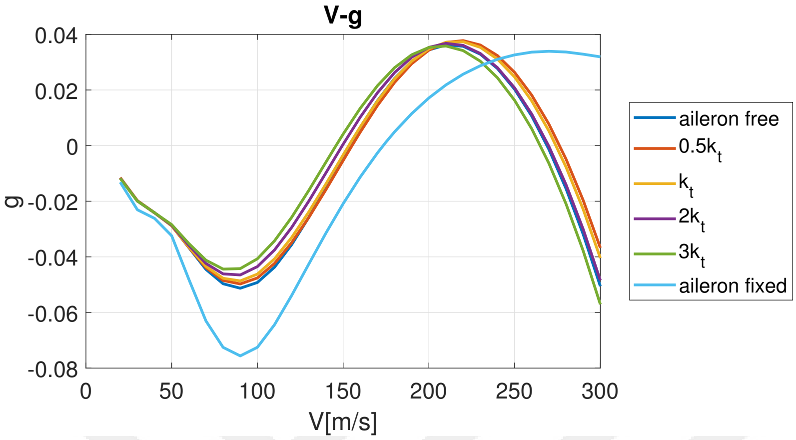

(a) Velocity vs Damping

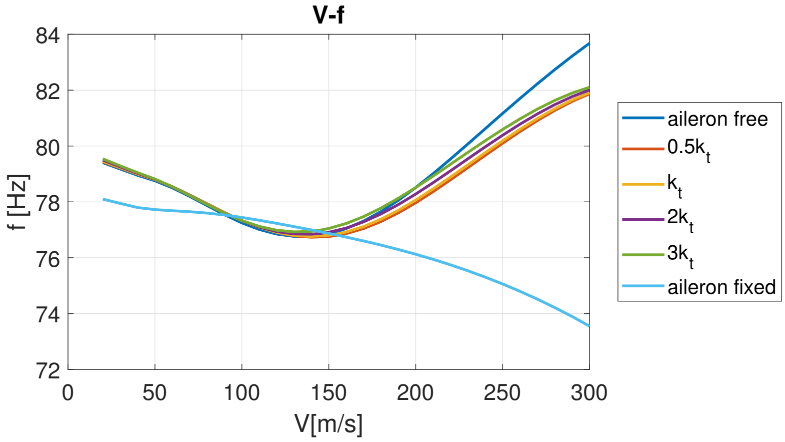

(b) Velocity vs Frequency

Figure 5.14: Damping and frequency graphs for the matched solution of the cantilevered wing model for different aileron stiffness cases

It can be seen from Figure 5.14a that the flutter speed of the fixed aileron case is higher than all other cases. Besides, Table 5.7 indicates that the critical speeds for the fixed and free cases are 173.4 m/s and 153.7 m/s, respectively. On the other hand, it is observed that the flutter speed decreases as the torsional stiffness of the aileron increases from 0.5k_t to 3.0k_t. Nevertheless, this trend does not mean that as the aileron stiffness increases further, the lowest flutter speed is seen when the aileron rotation is prevented. On the contrary, the highest flutter speed corresponds to the fixed aileron case since the coupling of the aileron with the wing mode is eliminated.

Here the unstable mode refers to the torsional deformation of the wing. However, for all cases except the one in which the aileron is fixed, the wing torsion is coupled with the aileron rotation. Figure 5.15 illustrates the flutter modes shapes obtained with the models that allow and do not allow the aileron rotation. In Figure 5.15a, the plot corresponding to the case with the assumed aileron stiffness of k_t is given as an example, but the mode shape is the same for all other cases except the fixed aileron one. Indeed, it can be seen from Table 5.7 that the flutter frequencies of the first five models are almost the same.

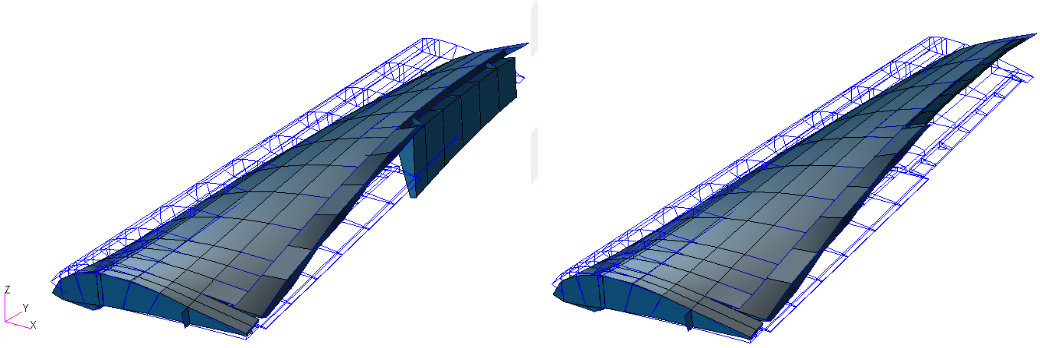

(a) Assumed aileron stiffness of k_t

(b) Fixed aileron

Figure 5.15: Flutter mode shapes of the wing

5.4.2 Flutter Analysis of the Aircraft Model

The free aircraft model is analyzed at the sea level, incompressible flow, i.e., Mach 0.0 condition. Firstly, modal analysis is carried out and the frequency of the first elastic mode is found to be 7 Hz. Dimensionless parameter reduced frequency is provided in a range calculated by taking the minimum and the maximum frequencies as 5 Hz and 60 Hz, the maximum and the minimum velocities as 20 m/s and 300 m/s.

In the normal modes analysis, some local modes are observed that are related to the concentrated mass elements and their connectivity to the structure. The local modes are excluded in the flutter analyses in order to get more realistic results.

The effect of coupling the bridging plate on flutter characteristics is examined in Table 5.8 and almost no change in flutter speed and flutter frequency is observed. The primary run expression in Table 5.8 refers to the initial flutter analysis in which the velocity set is specified with increments of 10 m/s. Consequently, the flutter velocities on the primary run columns are obtained from linear interpolation between 170 m/s and 180 m/s. A secondary analysis is also run by including additional data points around the velocity at which instability occurs. In this way, the linear interpolation is performed in a narrower range, between 177 m/s and 178 m/s, to calculate the flutter speed for the secondary run. To sum up, Table 5.8 indicates both that splining the wing bridging plate is not effective on the flutter outputs and that the initial and the additional interpolations result in really close values in this case.

Table 5.8: Flutter results with and without aeroelastic coupling of the wing bridging plate

	Wing Bridge Not Splined		**Wing Bridge Splined**	
	Primary Run	Secondary Run	Primary Run	Secondary Run
V_f [m/s]	178.29	177.91	178.69	177.93
f_f [Hz]	47.68	47.68	47.64	47.64

The velocity at which the damping is exactly equal to zero is found as 178.69 m/s by linear interpolation. The solution is obtained for Mach 0.0 at the sea level condition. The 178.69 m/s speed corresponds to Mach 0.526 at sea level, which does not match with the input Mach number. Thus, the flutter analysis is repeated with the input Mach number of 0.526 and the iterative analysis are performed until the input and resultant Mach numbers converge. Hence, the matched flutter solution is found as 199.4 m/s , Mach 0.586 at sea level. Figure 5.16 shows the damping and frequency graphs of the unstable mode obtained from the matched solution.

Between 130 m/s and 200 m/s, damping and frequency values fall outside the trends of the rest of the curves. When the mode shapes at that frequencies are checked, it is seen that they are not local modes to be excluded in the dynamic analysis. Therefore, flutter plots are given without omitting these extreme data points corresponding to aircraft level modes.

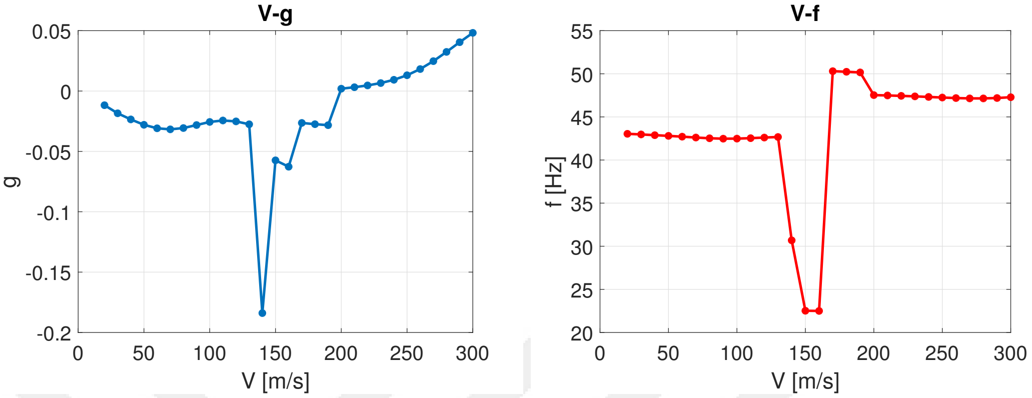

(a) Velocity vs Damping

(b) Velocity vs Frequency

Figure 5.16: Variation of damping and frequency for the matched solution of the full aircraft model with assumed aileron stiffness of $2k_t$

Zero structural damping is assumed in this case, but structural damping of 0.02 is considered a realistic estimation in general. Nevertheless, it is seen that as velocity further increases, damping reaches positive values much greater than 0.02. As a result, it is not possible to expect the instability to be covered by the structural damping and this mode is referred to as unstable.

The flutter mode shape is illustrated in Figure 5.17. It comprises the coupling of the in-plane and out-of-plane bending of the wings together with the symmetric horizontal tail bending and in-plane vertical tail bending.

Figure 5.16 demonstrates the flutter results for the aileron stiffness is k_t. It is seen in Figure 5.16b that first, the frequency is about 42 Hz and then switches to approximately 47 Hz. These correspond to the 23rd and the 26th normal modes with 43.18 Hz and 47.98 Hz modal frequencies, respectively. When the aileron stiffness is doubled, these two modes undergo flutter separately, as shown in Figure 5.18. In mode 23, flutter is observed at 229.0 m/s speed and 42.0 Hz, whereas flutter speed and frequency

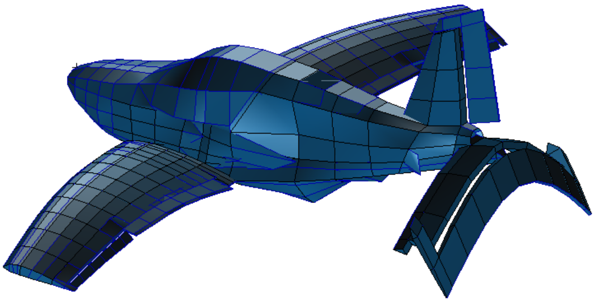

Figure 5.17: Flutter mode shape

of mode 26 are 222.6 m/s and 47.4 Hz, respectively, for 0.0 Mach number and sea level condition. In Table 5.9, flutter results are given for different values of aileron rotational stiffness.

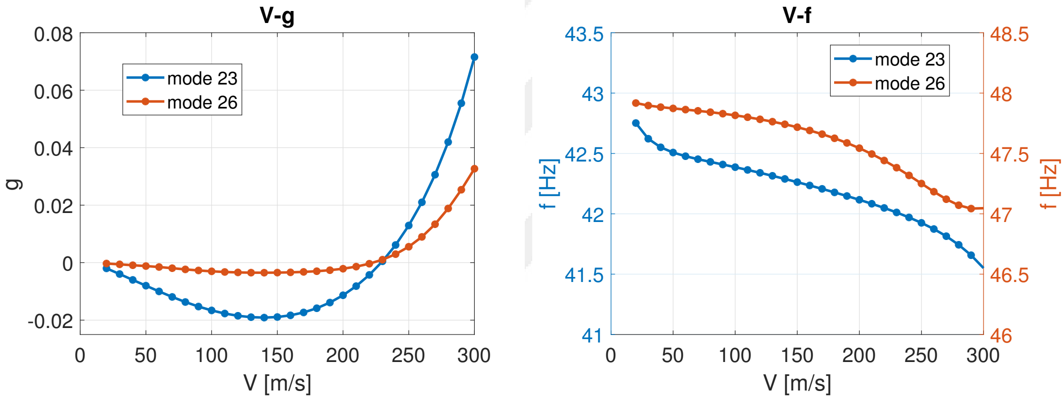

(a) Velocity vs Damping

(b) Velocity vs Frequency

Figure 5.18: Variation of damping and frequency with the velocity for the aileron stiffness of $2k_t$

Table 5.9 indicates that the lowest flutter speeds are seen for the lowest aileron stiffness values. However, it is not possible to say that as the aileron stiffness increases, flutter speed keeps increasing. Fixed aileron and $3.0k_t$ cases do not obey this trend. When the aileron is fixed, only mode 26 appears in the unstable point. Considering the variation of the frequency of the unstable points with the velocity, in all cases except the fixed blade and $2k_t$, it is seen that a frequency of about 42 Hz appears at low speeds, then some other modes interfere and finally, the frequencies become about 47 Hz. It is interpreted from this situation and from the results given in Table 5.9 that

Table 5.9: Sea level flutter analysis outputs for different aileron stiffness

Aileron	**Mach 0.0 Solutions**			**Matched Solutions**		
Stiffness	V_f [m/s]	f_f [Hz]	M_f	V_f [m/s]	f_f [Hz]	M_f
aileron free	199.7	47.6	0.587	180.0	47.6	0.529
$0.5k_t$	189.8	47.6	0.558	180.0	47.6	0.529
k_t	178.7	47.6	0.525	199.4	47.5	0.586
$2.0k_t$ (mode23)	229.0	42.0	0.673	214.1	42.3	0.630
$2.0k_t$ (mode 26)	222.6	47.4	0.654	234.5	47.0	0.690
$3.0k_t$	169.3	47.7	0.498	173.9	47.6	0.511
aileron fixed	192.6	47.60	0.566	215.2	47.3	0.633

different aileron stiffnesses bring different mode interferences, and these couplings may work both in a way, making the system more prone to flutter or postponing the flutter boundary. Therefore, a regular relation between the aileron stiffness and the flutter speed can not be obtained in this case. However, in any case, flutter speed is found to be 180 m/s or greater, which is really high considering the VLA's flight envelope.

The flutter mode shape of the cases with a flutter frequency of about 47 Hz is as in Figure 5.17. For the $2k_t$ case, mode 23 has the lowest matched flutter speed. Therefore, the mode shape at 42.3 Hz frequency is illustrated in Figure 5.19. It is seen that anti-symmetric wing bending is coupled with the aileron rotation. Unexpected deformations in the fuselage draw attention in Figures 5.17 and 5.19. It is thought that these behaviors of the fuselage members will be prevented in the real case. The important point here is that the displacements of the lifting surfaces are dominant in the flutter mode shapes, not that of the fuselage. Besides, there are no splines at the fuselage. Therefore, these excessive displacements are not transferred to the aerodynamic mesh.

Tables 5.9 and 5.7 indicate that flutter speeds found for the full aircraft are greater than the isolated wing. For both models, the fixed aileron case leads to a higher flutter speed than the free aileron case. Although a decrease in the wing flutter speed

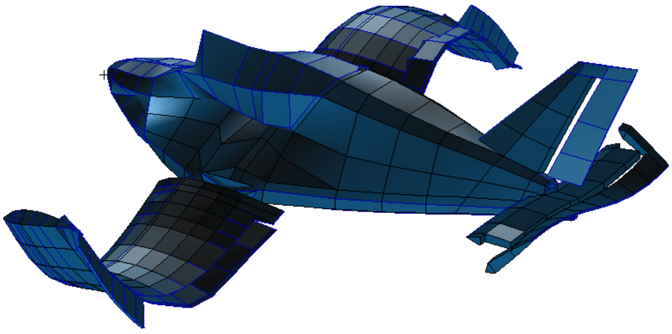

Figure 5.19: Flutter mode shape for aileron stiffness of $2k_t$.

is observed between the torsional stiffness of $0.5k_t$ and $3.0k_t$, a regular trend is not seen for the full aircraft model.

Finally, flutter solution at different altitudes is examined. Up to now, outputs of the sea level analyses are discussed. Flutter analysis at 1875 ft, 3750 ft, 5625 ft and 7500 ft are also performed with the aileron stiffness of k_t and the flutter Mach number versus altitude plot is given in Figure 5.20a. It is shown in Figure 5.20a that the flutter Mach number remains almost constant up to 3750 feet, then, it increases with the increasing flight altitude. Considering the Mach number and altitude relation given in the book named "A Modern Course in Aeroelasticity" [37] and shown in Figure 5.20b, the results of the current study are thought to be compatible with the expected trend.

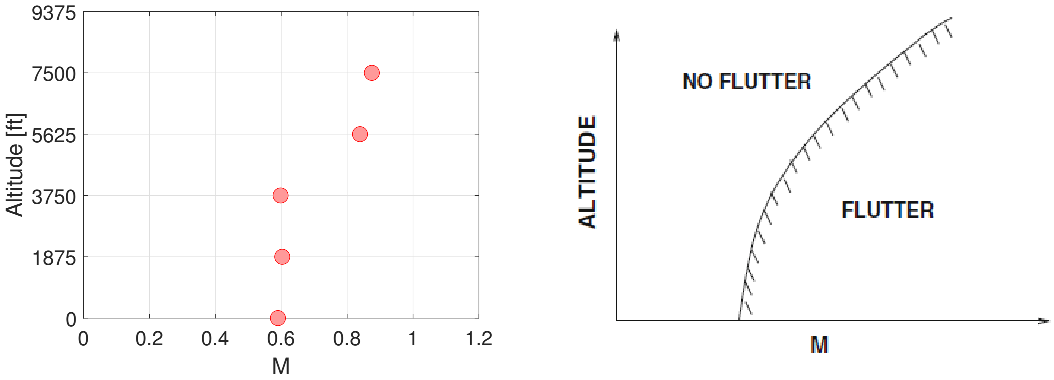

(a) Results obtained from the current study

(b) Relation given in [37]

Figure 5.20: Relation between flutter Mach number and altitude

5.5 Discrete Gust Response Results

Discrete gust response analysis is conducted by using the dynamic aeroelasticity solution sequence of Nastran, SOL 146. Besides the static aeroelastic analysis, the symmetrical boundary condition is applied to the CG of the model in this analysis, as previously explained.

Gust condition is defined as described in CS-VLA [1], which assumes the aircraft to be subjected to symmetrical, vertical gusts in level flight. The relevant paragraph of CS-VLA defines the gust shape and gust velocities as follows:

$$U = \frac{U_{de}}{2}(1 - cos\frac{2\pi s}{25\bar{c}}) \tag{5.1}$$

where U_{de} is the gust velocity specified as 15.24 m/s and 7.62 m/s at cruise and dive speeds, respectively, s is the distance penetrated into gust and $\bar{c}$ is the mean geometric chord of the wing. Figure 5.21 shows the 1-cosine gust shape defined in the analyses.

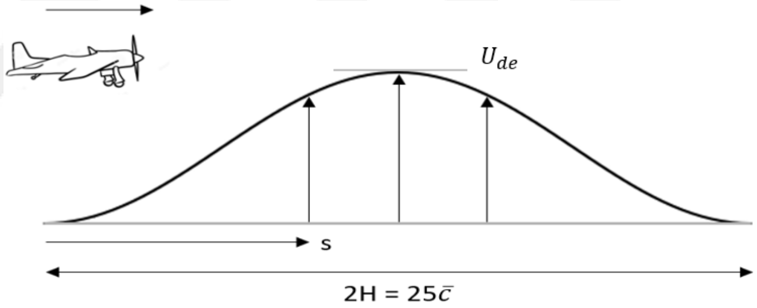

Figure 5.21: Discrete 1-cosine gust shape

Discrete (1-cosine) waveform gust with a single gust gradient length H of 12.5$\bar{c}$ at 7500 feet altitude is considered here. Figure 5.22 illustrates the gust profile at cruise and dive speed conditions. The indicated cruise and dive airspeeds are 56.6 m/s and 70.7 m/s, respectively. The transient response of the model to the 1-cosine gust is given in Figures 5.23 and 5.25.

Acceleration of the airplane is a desired output of gust response analysis and it can be critical for low-weight air vehicles. Transient response of vertical acceleration of the VLA for positive and negative gust encounters at cruise and dive speeds at 7500 feet is plotted in Figure 5.23 for the case in which the lifting surface connecting

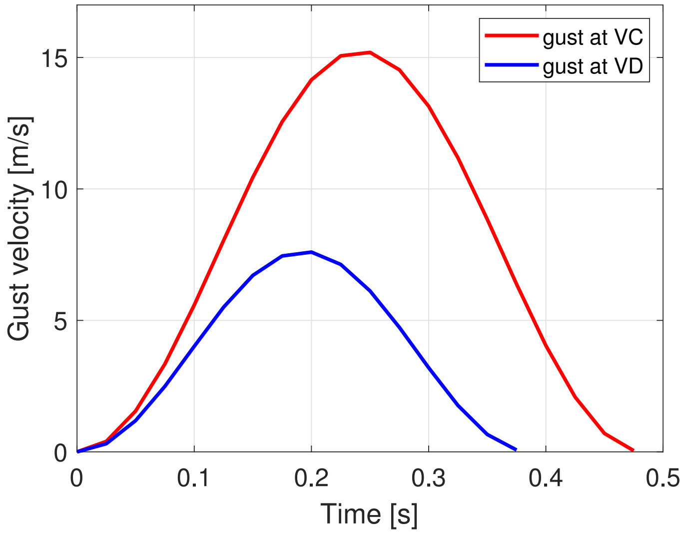

Figure 5.22: 1-cosine gust profile at cruise and drive speeds

the wings is splined to the structure. Positive 4.15g and negative 2.15g maximum accelerations are observed for the gust at the cruise speed. Analyses conducted at the cruise speed resulted in higher responses than that of dive speed since gust velocity at V_C is higher. Gust input is provided such that the air vehicle encounters the gust at t=0.2 seconds. When only the additional contribution due to gust is considered, positive and negative gusts result in responses equal in magnitude and opposite in sign. However, the corresponding values at the steady flight are added to the gust responses and plotted here. Therefore, in the below Figures, the values before t=0.2s, the instant gust initiates, represent the results obtained from 1g steady level flight.

The effect of splining the wing bridging panel on the gust response is also examined. Table 5.10 indicates that coupling the wing bridging plate with the structure amplifies the acceleration response.

Since a vertical gust is considered, vertical shear force and vertical bending moment responses are also investigated at the wing root. For the wing root shear force, a quadrilateral shell element located at the front spar web is selected. To check the bending moment effect, the change in the axial force of the bar element located at the front spar upper flange is examined. In Figure 5.24, structural entities selected to investigate the internal loads at the wing root are shown.

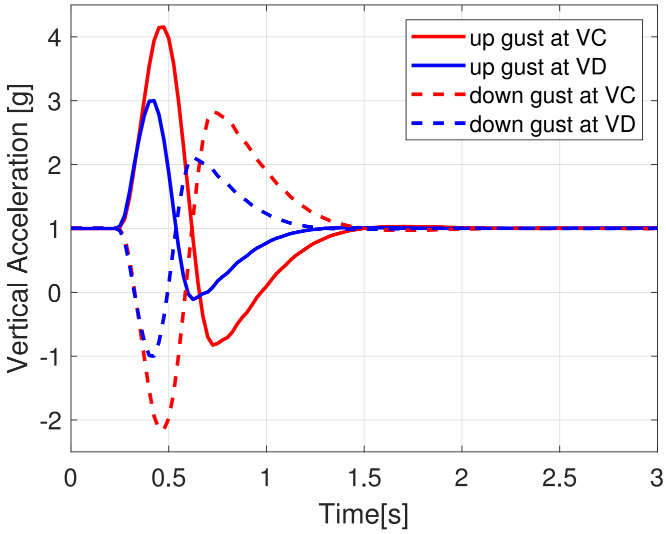

Figure 5.23: Gust response of vertical acceleration at the CG when the wing bridging plate is splined to the structure

Table 5.10: Acceleration response with and without aeroelastic coupling of the wing bridging plate

	Wing Bridge Not Splined	Wing Bridge Splined
Max. (+) acceleration	3.65 g	4.15 g
Max. (-) acceleration	1.65 g	2.15 g

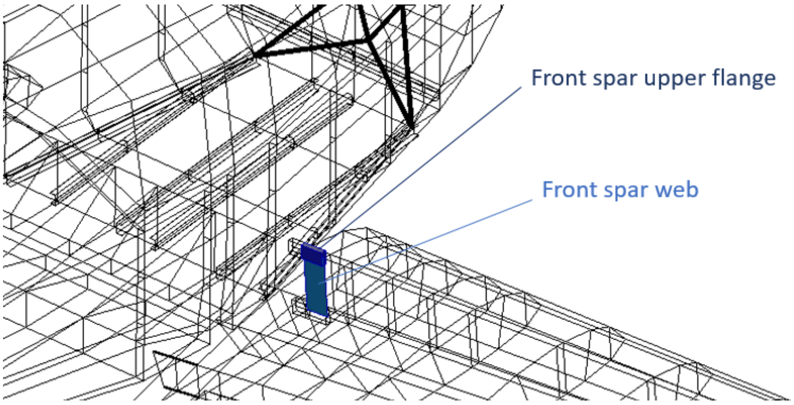

Figure 5.24: Front spar upper flange and web elements at the wing root

As seen in Figure 5.25, positive gust causes a negative axial force response initially; since the upper flange element is examined, it undergoes compression. It can be concluded that the loading increases significantly compared to the initial steady values in a short time and then, response dies out in about 1.5 seconds.

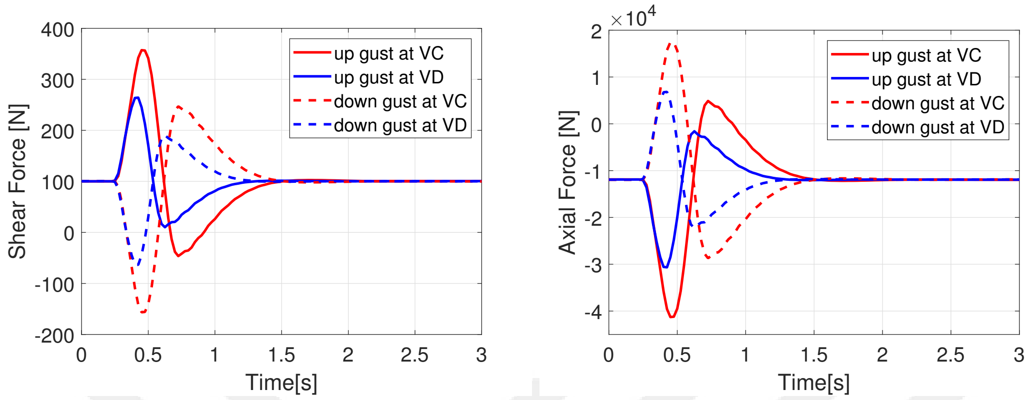

(a) Shear force at wing root front spar web

(b) Axial force at front spar upper flange

Figure 5.25: Gust response of the internal loads at the wing root

5.5.1 Tuned Gust Response

CS-VLA [1] defines gust condition at a single gust gradient length H of $12.5\bar{c}$. 12.5 times mean geometric chord makes 15.287 meters in this case. Gust velocities are given for this gradient length. Various gust gradient lengths are applied to V_C condition case because critical responses originate from that condition, and the up gust direction is chosen. Analysis flow of MSC.Nastran for discrete gust response calculations is demonstrated in Figure 5.26. $(\frac{H}{350ft})^{\frac{1}{6}}$ attenuation factor is seen in the flowchart. Tuned discrete gust approach is required both in FAR-25 [10] and CS-25 [38], and 30-350 feet gust gradient length range is mentioned. Reference gust velocity is taken at H=350 ft and $(\frac{H}{350ft})^{\frac{1}{6}}$ alleviating factor is applied to decrease gust velocity as gradient length reduces.

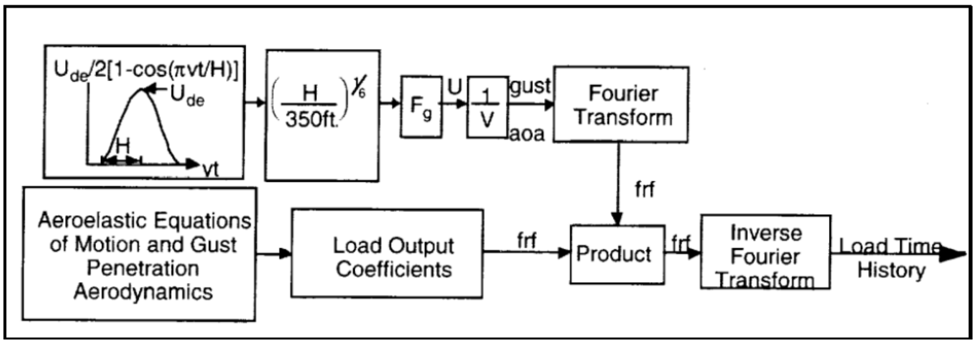

Figure 5.26: Analysis flow for MSC Nastran discrete gust response computations, from [8]

In this case, reference gust velocity is defined for H=15.287m. Therefore, $(\frac{H}{15.287m})^{\frac{1}{6}}$ factor is applied to decrease gust velocity for lower gust gradient lengths and increase gust velocity for greater gradient lengths. 1-cosine gust profiles are plotted in Figure 5.27 at a range of H=10m to H=110m. Each curve represents a gust profile with a different gust gradient length. Gust profile with gradient length of 10 meters is shown in red, where that of 110 meters is shown in black. Moreover, the reference case with H=12.5$\bar{c}$, is emphasized with markers. As the color gets darker, the gust gradient length increases. Change in maximum gust speeds can be seen in Figure 5.27.

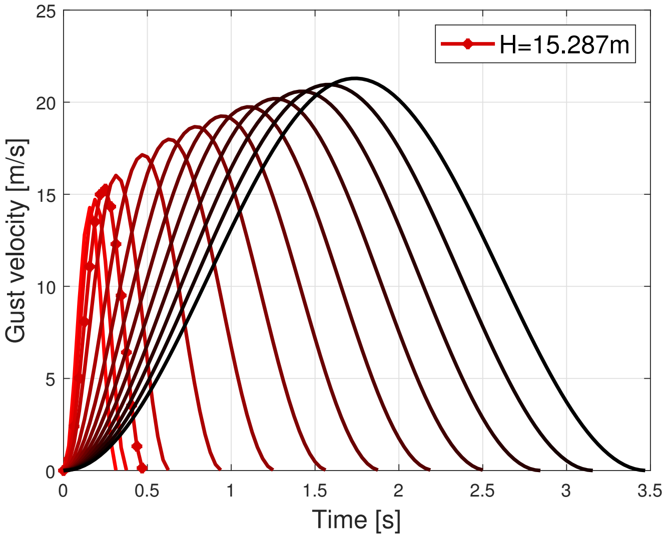

Figure 5.27: 1- cosine discrete gust velocities at various gust gradient lengths

Tuned discrete gust responses of acceleration, wing root shear force and flange axial force are shown in Figures 5.28, 5.30 and 5.32. The additional contribution of gust is plotted. Therefore, the response values in Figures 5.28, 5.30 and 5.32 are equal to zero before t=0.2 seconds. For each type of response, secondary plots showing response points of the highest magnitudes are given by adding more data points around H=12.5$\bar{c}$. Figures 5.29, 5.31 and 5.33 indicate the maximum load and the absolute value of the minimum load for each of the gradient lengths.

It is seen from Figure 5.29 that the highest positive acceleration response appears for H=12m and the highest absolute value of minimum acceleration is observed when H=30m. Since the positive response is critical here, gust gradient length of 12m is noted. However, there is only a slight difference between H=12m and H=15.287m, which is 3.15g vs. 3.21g contributional gust acceleration.

Similarly, wing root shear force response is greater at H=12m for the positive response and greater at H=30m for the absolute minimum response. Again H=12m gives the most critical output. Lastly, for the wing root, axial force response at the upper flange, the highest positive response shows up when H=30m and the highest absolute value of minimum response appears at H=12m. In contrast to acceleration and shear force responses, the absolute negative response is the critical one for axial force, and the gust gradient length of 12 meters points out the most severe condition for all three types of responses.

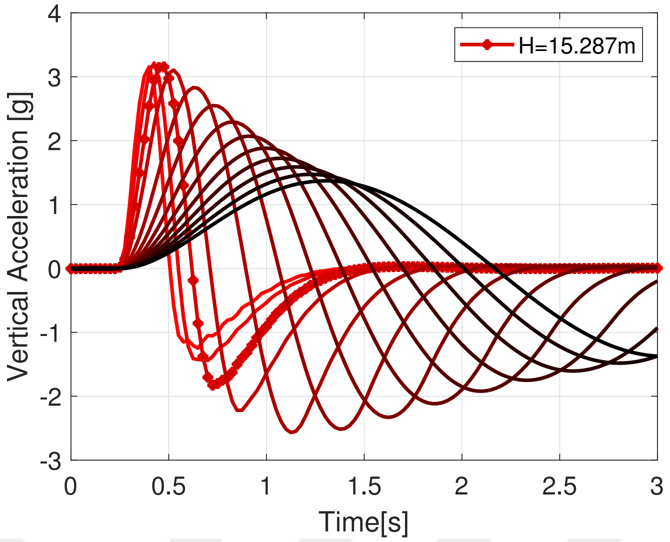

Figure 5.28: Tuned gust responses of acceleration figure

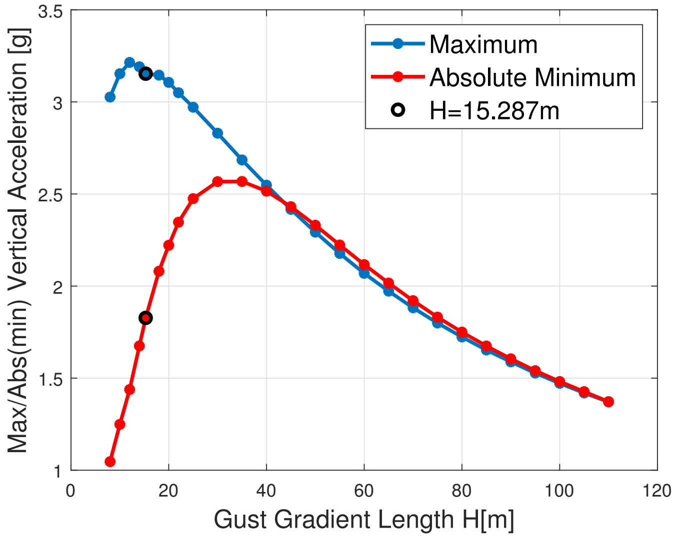

Figure 5.29: Maximum acceleration

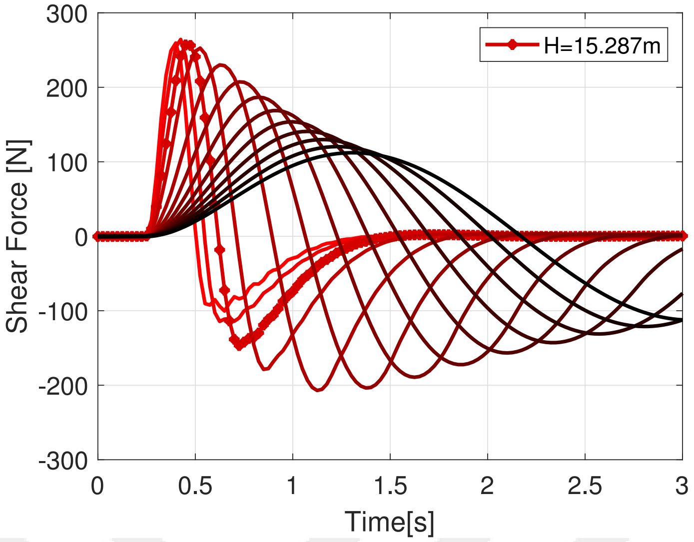

Figure 5.30: Tuned Gust response of shear force

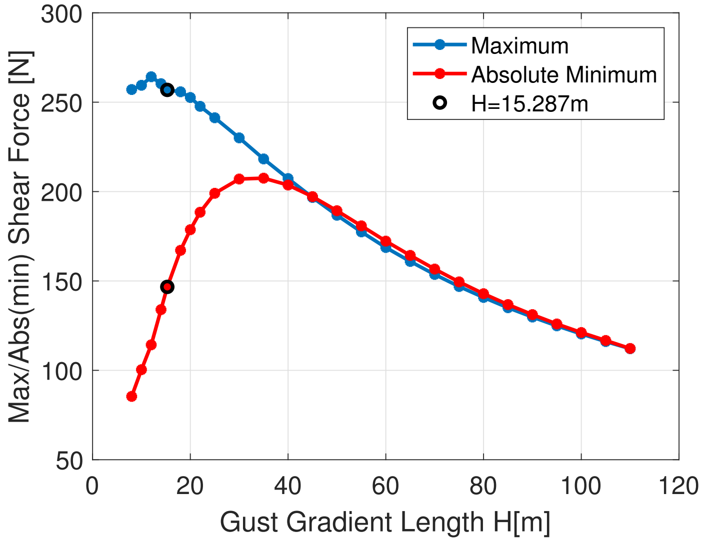

Figure 5.31: Maximum shear force

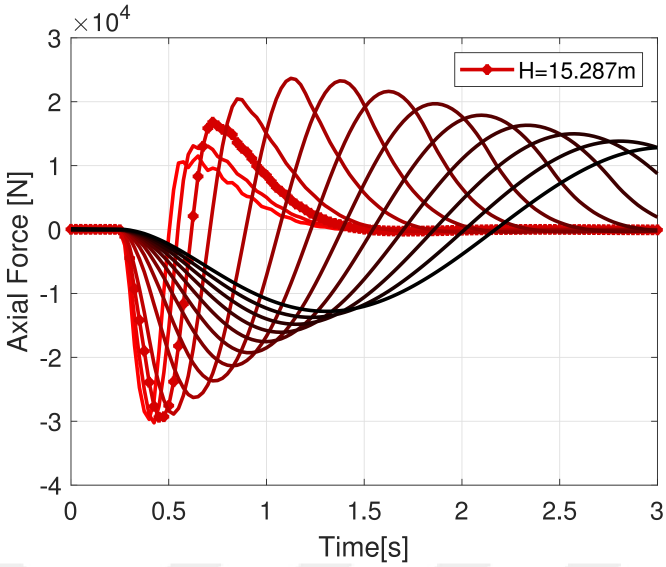

Figure 5.32: Tuned gust response of flange axial force

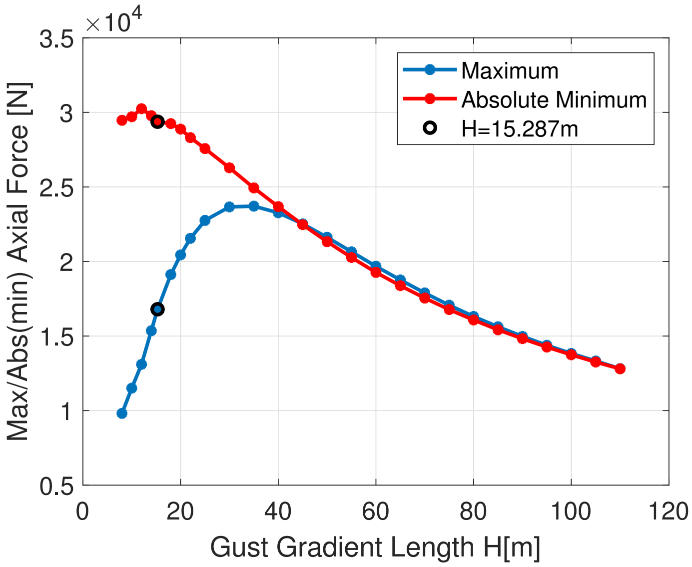

Figure 5.33: Maximum axial force

CHAPTER 6

CONCLUSIONS

Static aeroelastic, dynamic aeroelastic stability and dynamic response characteristics of a very light aircraft are investigated in this thesis by utilizing MSC.FlightLoads and MSC.Nastran. All types of aeroelastic analyses are first applied on the AGARD 445.6 wing and results are found to be compatible with the literature.

In static aeroelasticity, without the need to use another external program for aerodynamic calculations, distributed aerodynamic pressure loads are obtained to analyze the structure for a critical case. Static aeroelasticity leads to more realistic results as the aerodynamic loads take the structural deformations into account. In this study, camber and incidence of the wing are included in aerodynamic calculations of Nastran by imposing initial downwash to the wing aerodynamic mesh. It is showed that the DLM correction considerably influences the pressure distribution and results in a relatively closer distribution to CFD compared to the initial DLM result. Then, a couple of modeling approaches about the gap between the wings in the absence of the fuselage aerodynamic model are discussed. It is concluded that bridging the gap with an aerodynamic panel and splining the panel to the structure gives the most favorable result, in this case. Finally, outputs of the static trim analyses are examined in detail. It is seen that when wing incidence angle and camber is considered, greater aerodynamic forces are generated over the wings and the aircraft is trimmed at a lower angle of attack and elevator rotation. The maximum value of the pressure calculated on the aerodynamic mesh is decreased and the pressure distribution over the wings is changed significantly. One of the motivations of this study is the inquiry if we can reduce the dependency on higher-order solutions for structural purposes by effectively using this commercial tool in hand. Thus, the response of the structure under the CFD-based and DLM-based loads are compared by looking at the wing tip displacement and von Mises stress distribution over the wing. It is seen from this comparison that the practical and fast results obtained by Nastran are not too off from the CFD-based results. Although there are deviations between the compared results, the reason for the difference is interpretable and most importantly, Nastran outputs stand on the conservative side, which is acceptable at the preliminary design phases.

Secondly, the dynamic aeroelastic stability of the isolated wing and full aircraft models are analyzed. The change in flutter outputs with various aileron stiffness values is also presented. The wing flutter analysis shows that the highest flutter speed is observed when the rotation of the aileron is prevented. Moreover, the flutter speed of the aircraft is found around 200 m/s for the assumed aileron stiffness at sea level. CS-VLA [1] requires analysis to show that the aircraft is free from flutter for all speeds up to 1.2 V_{D} where V_{D} of the analyzed VLA is 70.7 m/s. It is indicated in this study that although different flutter speeds are found for various aileron stiffness, even the lowest critical speed is far beyond the flight envelope. Moreover, flutter analysis is repeated in a range of 0 feet to 7500 feet altitude. It is observed that the flutter Mach number increases with the increasing altitude.

Finally, in the dynamic response analysis part, discrete (1-cosine) waveform, positive and negative gusts at cruise and dive flight speeds are considered and transient response of the aircraft is found. The acceleration response at the CG of the aircraft and the internal structural loads response at the wing root are examined. It is seen that gust encounters at the cruise speed condition result in more critical responses. The maximum positive acceleration response is observed as 4.15 g for upward gust at V_{C} and the absolute maximum negative acceleration response as -2.15g for downward gust at V_{C}. Considering that the positive and negative limit maneuvering load factors of the VLA are 3.8g and -1.5g, respectively, gust load factors at the cruise speed are found to be more critical. By checking the gust response of the internal loads at the wing root, it is seen that when gust initiates, internal loads increase significantly compared to the initial steady values and then responses die out, as in the acceleration response, and the model exhibits dynamically stable behavior. The initial dynamic response analyses are for the case with a single gust gradient length of $H=12.5\bar{c}$. In tuned gust analysis, various gust gradient lengths are analyzed and the amplitude of gust excitation is tuned so that the gust velocity is reduced with an attenuation factor as the gust gradient length decreases. As a result, slightly higher responses than those found for the single gust gradient length required by CS-VLA [1] are captured at a shorter gradient length.

This thesis presents a single case for each type of aeroelastic analysis. However, to ensure the aeroelastic stability of an aircraft, analyses should cover the combinations of possible configurations and flight conditions. As future work, aircraft at different mass states can be analyzed for an extended range of flight parameters. Furthermore, aeroelastic modeling of the fuselage can also be included for a more realistic approach. Lastly, this study covers only the effect of aileron rotational stiffness on the flutter results. This investigation can be expanded by including the other control surfaces as well.

REFERENCES

[1] EASA, *Certification Specifications for Very Light Aeroplanes*. 2003.

[2] J. R. Wright and J. E. Cooper, *Introduction to Aircraft Aeroelasticity and Loads: Second Edition*. 2015.

[3] D. Howe, *Aircraft Loading and Structural Layout*. AIAA education series, Professional Engineering Publishing, 2004.

[4] R. L. Bisplinghoff, H. Ashley, and R. L. Halfman, *Aeroelasticity*. New York: Dover Publications, 1955.

[5] L. Bairstow and A. Fage, "Oscillations of the tailplane and body of an aircraft in flight," *ARC R&M 276, part 2*, 1916.

[6] F. Lanchester, "Torsional vibration of the tail of an airplane," *ARC R&M 276, part 1*, 1916.

[7] O. V. Team, "ODTÜ Very Light Aircraft Project Preliminary Design Report," tech. rep., 2021.

[8] A. S. Naser and A. S. Pototzky, "Response of the Alliance 1 Proof-of- Concept Airplane Under Gust Loads," Tech. Rep. March, 2001.

[9] S. Özöztürk, A. Kayran, N. Alemdaroglu, and G. Seber, "On the Design and Aeroelastic Stability Analysis of Twin Wing-Tail Boom Configuration Unmanned Air Vehicle," *AIAA*, no. April, pp. 1–42, 2014.

[10] FAA, *Airworthiness Standards: Transport Category Airplanes*. 2003.

[11] E. Albano and W. P. Rodden, "A doublet-lattice method for calculating lift distributions on oscillating surfaces in subsonic flows.," *AIAA Journal*, vol. 7, no. 2, pp. 279–285, 1969.

[12] J. P. Giesing, T. P. Kalman, and W. P. Rodden, "Subsonic Unsteady Aerodynamics for General Configurations Part I, Vol I - Direct Application Of The Nonplanar Doublet-Lattice Method," tech. rep., Air Force Flight Dynamics Laboratory, 1971.

[13] J. P. Giesing, T. P. Kalman, and W. P. Rodden, "Subsonic Unsteady Aerodynamics for General Configurations Part II Volume II - Computer Program N5KA," tech. rep., Air Force Flight Dynamics Laboratory, 1972b.

[14] J. P. Giesing, T. P. Kalman, and W. P. Rodden, "Subsonic Unsteady Aerodynamics For General Configuraitons - Part II, Vol I - Application of the Doublet-Lattice Method and the Method of Images to Lifting-Surfaces/Body Interface," tech. rep., Air Force Flight Dynamics Laboratory, 1972a.

[15] J. P. Giesing, T. P. Kalman, and W. P. Rodden, "Subsonic steady and oscillatory aerodynamics for multiple interfering wings and bodies," *Journal of Aircraft*, vol. 9, no. 10, pp. 693–702, 1972c.

[16] C. Reschke and T. Kier, "An Integrated Model for Aeroelastic Simulation of large flexible Aircraft using MSC. Nastran," pp. 1–13, 2004.

[17] J. K. Dillinger, M. M. Abdalla, Y. M. Meddaikar, and T. Klimmek, "Static Aeroelastic Stiffness Optimization of a Forward Swept Composite Wing with CFD-Corrected Aero Loads," *CEAS Aeronautical Journal*, vol. 10, no. 4, pp. 1015–1032, 2019.

[18] E. Yates, J. Foughner, N. Land, and NASA., *Measured and Calculated Subsonic and Transonic Flutter Characteristics of a 45 Degree Sweptback Wing Planform in Air and in Freon-12 in the Langley Transonic Dynamics Tunnel*. NASA TN D-1616, NASA, 1963.

[19] E. Yates, *AGARD Standard Aeroelastic Configurations for Dynamic Response. Candidate Configuration I.-wing 445.6*. Defense Technical Information Center, 1987.

[20] R. M. Kolonav, *Unsteady Aeroelastic Optimization In The Transonic Regime*. PhD thesis, Purdue University by, 1996.

[21] J. Cai, F. Liu, H. Tsai, and A. Wong, *Static Aero-elastic Computation with a Coupled CFD and CSD Method*. 2001.

[22] M. Förster and C. Breitsamter, “Aeroelastic prediction of discrete gust loads using nonlinear and time-linearized cfd methods,” *Journal of Aeroelasticity and Structural Dynamics*, vol. 3, no. 3, 2015.

[23] MSC.Software Corporation, *MSC.FlightLoads and Dynamics User’s Guide*. 2006.

[24] J. Cecrdle and V. Hlavaty, “Aeroelastic Certification of Light Sport Aircraft According "LTF" Regulation,” in *18th International Conference ENGINEERING MECHANICS 2012*, 2013.

[25] J. Dimitrijević and P. Kovačević, “Computational Modal Analysis of the LASTA Aircraft,” *Scientific Technical Review*, vol. 60, no. 1, pp. 60–69, 2010.

[26] E. H. Johnson and W. P. Rodden, *MSC Nastran Aeroelastic Analysis User’s Guide*. 2004.

[27] Z. T. Inc., *ZAERO User’s Manual, Version 9.3*. 2019.

[28] A. Bagai, “Technical note: Definition of the mean camber line from airfoil shapes,” *Journal of The American Helicopter Society - J AMER HELICOPTER SOC*, vol. 51, 10 2006.

[29] Z. T. Inc., *ZAERO Theoretical Manual, Version 8.3*. 2008.

[30] J. Castro, “A review of splining for aero-structure coupling in aeroelastic solutions,” 2010.

[31] C. Riso, F. G. Di Vincenzo, M. Ritter, C. E. S. Cesnik, and F. Mastroddi, “Nonlinear aeroelastic trim of very flexible aircraft described by detailed models,” *Journal of Aircraft*, vol. 55, no. 6, pp. 2338–2346, 2018.

[32] R. H. Scanlan and R. A. Rosenbaum, *Introduction to the Study of Aircraft Vibration and Flutter*. Dover Publications New York, 1968.

[33] C. Irwin and P. R. Guyett, “The subcritical response and flutter of a swept-wing model,” 1965.

[34] W. Rodden, R. Harder, E. Bellinger, and L. R. Center, *Aeroelastic Addition to NASTRAN*. Aeroelastic Addition to NASTRAN, National Aeronautics and Space Administration, Scientific and Technical Information Branch, 1979.

[35] C. Vidy, L. Katzenmeier, M. Winter, and C. Breitsamter, “Verification of the use of small-disturbance cfd aerodynamics in flutter and gust analyses for simple to highly complex configurations,” in *International Forum on Aeroelasticity and Structural Dynamics*, 2015.

[36] B. Okumuş, “The effect of structural layout on the supersonic flutter characteristics of a fighter wing,” Master’s thesis, Middle East Technical University, 2018.

[37] R. Clark, D. Cox, H. CurtissJr, J. Edwards, K. Hall, D. Peters, R. Scanlan, E. Simiu, F. Sisto, T. Strganac, and E. Dowell, *A Modern Course in Aeroelasticity*. 01 2005.

[38] EASA, *Certification Specifications for Large Aeroplanes*. 2007.